PASJ: Publ. Astron. Soc. Japan **55**, 17–58, 2003 February 25

The Virgo High-Resolution CO Survey: I. CO Atlas

Yoshiaki SOFUE,[1] Jin KODA,[2] Hiroyuki NAKANISHI,[1] Sachiko ONODERA,[1]
Kotaro KOHNO,[1] Akihiko TOMITA,[3] and Sachiko K. OKUMURA[2]
[1]*Institute of Astronomy, The University of Tokyo, Mitaka, Tokyo 181-0015*
[2]*Nobeyama Radio Observatory, National Astronomical Observatory, Minamimaki, Minamisaku, Nagano 384-1305*
[3]*Faculty of Education, Wakayama University, Wakayama 640-8510*
sofue@ioa.s.u-tokyo.ac.jp

(Received 2002 September 4; accepted 2002 December 13)

Abstract

We present the results of the Virgo high-resolution CO survey (ViCS) obtained with the Nobeyama Millimeter-wave Array (NMA). This survey was made during the course of a long-term project at Nobeyama from 1999 December through 2002 April. The objects were selected from Virgo cluster members, while considering the CO richness from the single-dish flux, mild inclination, and a lack of strong tidal perturbations. The central $1'$ regions (~ 4.7 kpc) of 15 spiral galaxies were observed with resolutions of $2''$–$5''$ and 10–20 km s^{-1}, and sensitivities of ~ 20 mJy beam^{-1} for a 10 km s^{-1} channel. The objects lie at the same distance of the Virgo cluster (16.1 Mpc), which is advantageous for comparisons among individual galaxies. We describe the details of observations and data reduction, and present an atlas of integrated CO intensity maps, velocity fields and position–velocity diagrams along the major axes. The molecular gas morphology in the Virgo galaxies shows a wealth of variety, not specifically depending on the Hubble types. Several galaxies show a strong concentration of gas in the central few kpc region, where the CO morphology shows either a "single-peak" or a "twin-peaks". The morphology of more extended CO components can be classified into "arm-type", "bar-type", and "amorphous-type".

Key words: galaxies: ISM — galaxies: spiral — galaxies: structure — galaxies: Virgo Cluster of

1. Introduction

CO-line observations play an essential role in studying the kinematics and interstellar physics in the central regions of spiral galaxies, where the interstellar matter is mostly in the molecular-gas phase, and is strongly concentrated (Sofue et al. 1995; Honma et al. 1995). There have been numerous observations of nearby galaxies in the CO line emissions with single-dish telescopes (Young, Scoville 1991; Braine et al. 1993; Young et al. 1995; Nishiyama, Nakai 2001). Large-scale CO line surveys of the Virgo galaxies have been obtained using the FCRAO 14-m telescope at an angular resolution of $45''$ by Kenney and Young (1988), and the BTL 7-m telescope by Stark et al. (1986). These surveys with single dishes were made with angular resolutions of tens of arcsec, and have given information about the global structure of molecular disks in Virgo and nearby galaxies.

Interferometer observations at high angular resolutions are crucial for studying detailed molecular disk structures within the central few hundred parsecs (Sargent, Welch 1993). A high-spectral resolution is also crucial to investigate the detailed kinematics of the central gas disks. Both high spatial and high spectral resolutions provide us with precise velocity fields and rotation curves, which are the basis for deriving the fundamental parameters, such as the mass distribution, bars and related shock phenomena, triggering mechanism of starburst, and/or fueling mechanism of massive black holes. Interferometer observations have often been performed to investigate the individuality of each galactic center and activity. Recently, some large surveys of nearby galaxies have started to be reported.

The Nobeyama mm-wave Array (NMA) and Owens Valley Radio Observatory (OVRO) mm-wave array have been used since the 1990's to map the central regions of nearby spiral galaxies with the CO line at a typical angular resolution of $4''$ (Sakamoto et al. 1999a). The Berkely–Illinois–Maryland Association Survey of Nearby Galaxies (BIMA SONG) has mapped 44 nearby galaxies at typical resolutions of $6''$ (Regan et al. 2001). Interferometer observations of several nearby galaxies have also been conducted based on various interests, such as bars (e.g., Kenney et al. 1992), star formation (e.g., Wong, Blitz 2002), and nuclear activity (e.g., Baker 1999; Sakamoto et al. 1999a; Kohno et al. 1999; Schinnerer et al. 1999).

The ViCS (Virgo high-resolution CO survey) project with the NMA has been performed in order to obtain a homogeneous high angular- and spectral-resolution database for a large number of CO-bright Virgo Cluster spirals in the ^{12}CO (J = 1–0) line. The angular resolutions were $\sim 3''$ after reduction in the conventional CLEAN procedure with natural weighting. The major scientific motivation was to investigate the detailed central kinematics of the galaxies, particularly the innermost rotation curves from analyses of the position–velocity diagrams across the nuclei, which would be effective to detect central compact massive objects. The data are also useful to investigate the kinematics and ISM physics of the central molecular disks, and their environmental effect in the cluster circumstance.

An advantage to observe the Virgo Cluster galaxies is their almost identical distance, which has been accurately

Table 1. Object list for the high-resolution Virgo CO survey (ViCS).

NGC	Morphology	Activity	$B_{\rm total}$ [mag]	Opt. size [$'\times'$]	i [°]	PA [°]	$T_{\rm MB,peak}$ [mK]	$I_{\rm CO}$ [K km s^{-1}]	$V_{\rm CO}$ [km s^{-1}]	$\Delta V_{\rm CO}$ [km s^{-1}]
(1)	(2)	(3)	(4)	(5)	(6)	(7)	(8)	(9)	(10)	(11)
4192	SAB(s)ab	T2	10.95	9.8×2.8	74	155	38	8.9	−105	330
4212	SAc	H	11.83	3.2×1.9	47	75	53	7.5	−60	130
4254	SA(s)c	H	10.44	5.4×4.7	28	45	162	19.3	2407	200
4303	SAB(rs)bc	H	10.18	6.5×5.8	25	0	167	21.6	1555	160
4402	Sb	···	12.55	3.9×1.1	75	90	96	12.4	244	200
4419	SB(s)a	T2	12.08	3.3×1.1	67	133	80	18.5	−203	300
4501	SA(rs)b	S2	10.36	6.9×3.7	58	140	73	21.8	2263	450
4535	SAB(s)c	H	10.59	7.1×5.0	43	0	60	8.5	1949	250
4536	SAB(rs)bc	H	11.16	7.6×3.2	67	116	80	18.4	1793	310
4548	SBb(rs)	L2	10.96	5.4×4.3	37	150	44	6.7	450	210
4569	SAB(rs)ab	T2	10.26	9.5×4.4	63	23	124	26.5	−203	320
4571	SA(r)d	···	11.82	3.6×3.2	38	55	42	3.3	346	130
4579	SAB(rs)b	S1.9/L1.9	10.48	5.9×4.7	37	60	58	7.5	1465	380
4654	SAB(rs)cd	H	11.10	4.9×2.8	52	125	65	6.0	1075	180
4689	SA(rs)bc	H	11.60	4.3×3.5	30	160	51	6.5	1614	210

Notes. — Col. (1): Galaxy name. Col. (2): Morphological type from NED. Col. (3): Nuclear activity from optical spectroscopy (Ho et al. 1997a). H, S, L, and T stand for H II, Seyfert, LINER, and Transient-type (H II + LINER), respectively. Cols. (4) and (5): Total B-band magnitude and apparent sizes along major and minor axes, taken from NED. Cols. (6) and (7): Inclination and position angle of the major axes taken from Kenney and Young (1988). Cols. (8) and (9): CO Peak temperature and integrated intensity at optical centers taken from the FCRAO survey by Kenney and Young (1988), scaled to main-beam temperature by a scaling factor of $T_{\rm A}^*/T_{\rm MB} = 0.55$ for the FCRAO telescope (Young et al. 1995). Cols. (10) and (11): Intensity-weighted mean velocity and full width at 0% intensity of CO line from Kenney and Young (1988).

determined to be 16.1 Mpc ($1''$ corresponds to 78 pc) by the Cepheid calibrations (Ferrarese et al. 1996). Since our target galaxies lie within 2 Mpc from the Virgo center, M 87, the distance ambiguity will be at most 15%, mostly less than 10%. An accurate distance will enable us to estimate the various physical quantities rather precisely, such as the CO and dynamical masses, and the linear scales of the gas disks.

The ViCS results will be published in a series of papers. In this paper we describe the overall observations and reduction, and present an atlas of the central molecular disks of the Virgo galaxies. In forthcoming papers we will describe more details of the observations, analyses, and results for individual galaxies, as well as rotation curves and central kinematics, investigations of the ISM physics, and comparison with other wavelengths observations. The database will be opened for public use on our web page.

2. Observations and Reduction

2.1. Target Galaxies

The target galaxies in the survey have been selected from a list of spiral galaxies of the FCRAO CO-line survey by Kenney and Young (1988) by the following criteria:

1. The sources were chosen in the order of the CO line peak antenna temperatures, $T_{\rm A}^\star$(peak), at the optical centers. Twenty-eight galaxies with peak antenna temperatures above 20 mK were selected from 42 galaxies of Kenney and Young (1988).
2. The inclination angles were limited to be $25^\circ \le i \le 75^\circ$ in order to investigate the central gas dynamics. This criterion excluded NGC 4293 ($i = 76^\circ$), NGC 4302 ($i = 90^\circ$), NGC 4312 ($i = 78^\circ$), and NGC 4710 ($i = 90^\circ$).
3. Galaxies with the morphological type of S0, i.e. NGC 4293, NGC 4710, and NGC 4438, were excluded.
4. Interacting galaxies were excluded by a criterion that the galaxies have no companion within $8'$ radius. Pairs of NGC 4568/4567, NGC 4298/4302, and NGC 4647 were excluded.
5. Peculiar galaxies in optical images, i.e. NGC 4438 and NGC 4064, were excluded.
6. Galaxies observed with the NMA since 1994 were excluded. NGC 4321 and NGC 4527 have been observed by Sakamoto et al. (1999a,b) and Sofue et al. (1999a,b), respectively.

Sixteen galaxies were selected based on these criteria, and we have observed 15 galaxies, except NGC 4450. The targets are listed in table 1, which also summarizes the morphological type, B-band total magnitude, the optical size, inclination, position angle from optical isophotal contours, and the nuclear activity from optical spectroscopy (Ho et al. 1997a,b). The table also lists the CO-line peak temperature, integrated intensity, intensity-weighted mean velocity, and velocity width from single-dish CO-line observations (Kenney, Young 1988),

The selection criterion 1 (peak antenna temperature) was applied because of a higher probability to detect in a single channel. We note that the FCRAO survey with $45''$ resolution (Kenney, Young 1988) shows that all galaxies, except one, are centrally CO peaked. Their data show that the peak temperature and the maximum CO intensity have approximately a linear correlation, and that the CO scale radius is an increasing

Table 2. Observational parameters.

NGC	Config.	Year	Field center (4)		Frequency (GHz)	Reference
(1)	(2)	(3)	RA(J2000)	DEC(J2000)	(5)	(6)
4192	AB+C+D	2000–2002	12 13 48.30	+14 54 02.9	115.350000	1
4212	C+D	2000–2001	12 15 39.11	+13 54 04.8	115.286574	2
4254	AB+C+D	2000	12 18 50.03	+14 24 52.8	114.355710	3
4303	AB+C+D	2000	12 21 54.87	+04 28 24.9	114.659250	2
4402	AB+C+D	2001–2002	12 26 07.06	+13 06 45.7	115.200000	1
4419	AB+C+D	2000–2002	12 26 56.43	+15 02 51.1	115.286574	1
4501	AB+C+D	2001–2002	12 31 59.14	+14 25 12.9	114.407000	4
4535	AB+C+D	2000–2001	12 34 20.25	+08 11 52.2	114.507290	5
4536	AB+C+D	2001	12 34 27.07	+02 11 18.3	114.586000	5
4548	AB+C+D	2001	12 35 26.40	+14 29 47.0	115.098000	3
4569	AB+C+D	2000–2002	12 36 49.82	+13 09 45.8	115.286574	4
4571	C+D	2001–2002	12 36 56.40	+14 13 02.0	115.138000	3
4579	AB+C+D	2001–2002	12 37 43.53	+11 49 05.4	114.710000	6
4654	AB+C+D	2000–2002	12 43 55.74	+13 07 44.2	114.811630	1
4689	C+D	2000–2002	12 47 45.60	+13 45 46.0	114.659250	3

Notes. — Col. (1): Galaxy name. Col. (2): NMA configurations used for the observations. Col. (3): Year of the observations. Col. (4): Pointing position as well as the phase tracking center. Col. (5): Observing frequency. Col. (6): References for positions: (1) Condon et al. (1990); (2) Saikia et al. (1990); (3) NED; (4) Sakamoto et al. (1999a); (5) Hummel et al. (1988); (6) Kohno et al. (1999).

function of maximum CO intensity. This implies that our selection based on the peak temperature is approximately equivalent to a selection by the total integrated CO intensity, and hence based on the total CO luminosity for their equal distances. Hence, our target galaxies, and some that were not selected because they were already observed by NMA, would represent the most CO luminous Virgo galaxies.

2.2. *Observations*

We performed aperture synthesis observations of the ^{12}CO (J = 1–0) line emission from the 15 Virgo galaxies listed in table 1 during the course of a long-term project in the winter seasons of 2000 (1999 December–2000 April), 2001 (2000 December–2001 April), and 2002 (2001 December–2002 April). We made the observations in three available configurations: AB (long baselines), C (medium) and D (short) configurations. The visibility data covered projected baselines from about 10 to 351 m. The NMA consisted of six 10-m antennas, providing a field of view with a FWHP beam width of 65″ at 115 GHz. Table 2 lists the observation periods and array configurations, the observed central frequencies, and the positions of the pointing centers as well as the phase-reference centers for individual galaxies.

Since interferometry observations sample data in a Fourier space, the range of collected Fourier components, or baselines, determines the detectable sizes of objects. In our observations, the antenna size limited the minimum projected baseline length, restricting the largest detectable size to about 54″. Thus, our data may miss the fluxes of extended components of the objects with scales greater than this size, even if they are strong enough to be detected with single-dish observations. Also, the detectable flux depends on the r.m.s. noise of the resultant maps and, therefore, on the sensitivity of the array system. Hence, weak sources may be missed, even though their total flux as an ensemble is detectable by a single-dish low-resolution observations.

The antenna were equipped with tuner-less SIS receivers, which had receiver noise temperatures of about 30 K in double sidebands, and the typical system noise temperatures were about 400 K in the single sideband. We used a digital spectro-correlator system (Okumura et al. 2000), which had two spectroscopic modes (bandwidths of 512 and 1024 MHz); we used the mode covering 512 MHz (1331 km s^{-1}) with 256 channels and 2 MHz (5.2 km s^{-1}) resolutions.

The nearby radio point source 3C 273 was used as the flux and phase calibrator, which was observed every 20 min. The band-pass response across the channels was also calibrated using the 3C 273 data. The intrinsic flux density of 3C 273 at the observing frequency was calibrated for each observing run (typically 5 days) using the planets (Mars etc.). The flux of 3C 273 during the three-year observing periods was gradually variable between 9 and 12 Jy. The uncertainty in the absolute flux scale for each observing run was $\sim \pm 15\%$, which applies to all results presented in this paper.

2.3. *Reduction*

The raw data were calibrated using UVPROC-II, a first-stage reduction software, and were Fourier-transformed using the NRAO Astronomical Image Processing System (AIPS). We applied the CLEAN method with natural weighting to obtain three-dimensional data cubes (RA, DEC, $V_{\rm LSR}$). The intensity data were averaged in 2 to 6 bins (10.4–31.2 km s^{-1}) of the original channels in the spectro-correlator, and the channel increments were set to 2 to 4 (10.4–20.8 km s^{-1}). The intensity

Table 3. Parameters of cubes.

NGC	Synth. beam (2)			ΔV (km s^{-1})		N_c	R.m.s. for 10 km s^{-1} (6)		T_b for 1 Jy beam^{-1} (K)	$f_{45''}$ (%)
(1)	($''$)	($''$)	(°)	(3)	(4)	(5)	(mJy beam^{-1})	(mK)	(7)	(8)
4192	2.4	1.9	158	20.8	20.8	23	18	363	20.2	47
4212	4.0	3.7	149	20.8	10.4	22	28	174	6.2	76
4254	3.0	2.3	148	20.8	10.4	22	25	333	13.3	102
4303	2.8	1.9	27	10.4	10.4	17	21	363	17.3	97
4402	2.8	2.3	166	20.8	10.4	20	26	371	14.3	106
4419	3.5	2.7	159	10.4	10.4	38	26	253	9.7	83
4501	5.6	3.7	160	10.4	10.4	46	17	75	4.4	85
4535	3.1	2.6	164	10.4	10.4	23	21	240	11.4	208
4536	2.5	1.8	173	10.4	10.4	34	17	347	20.4	68
4548	2.6	2.0	154	31.2	15.6	19	22	389	17.7	16
4569	4.5	3.1	146	10.4	10.4	37	25	165	6.6	111
4571	3.8	2.5	154	31.2	15.6	0	33	319	9.7	...
4579	4.5	3.5	152	20.8	10.4	44	22	128	5.8	31
4654	5.2	3.7	149	20.8	10.4	23	22	105	4.8	142
4689	5.2	4.2	134	20.4	10.4	17	20	84	4.2	68

Notes. — Col. (1): Galaxy name. Col. (2): Major and minor axis sizes and position angle for the synthesized beam. Cols. (3) and (4): Integrated velocity width of a channel, and sampling width between channels of the cube. Col. (5): Number of channels where emission are detected. Col. (6): R.m.s. noise scaled for a 10 km s^{-1} channel. Col. (7): Equivalent antenna temperature for 1 Jy beam^{-1}. Col. (8): Fraction of single-dish flux recovered by the aperture synthesis observations. Single-dish data are from Kenney and Young (1988).

scale at this stage was in Jy per synthesized beam, which can be converted to brightness temperature in Kelvin. The resultant synthesized beam sizes range in $2''$–$5''$. The typical r.m.s. noise scaled for a 10 km s^{-1} channel was 20 mJy beam^{-1}. Table 3 lists the resultant parameters of the data cubes for individual galaxies.

In addition to the above reduction parameter set, we CLEANed the data with tapered and uniform weighting functions, which provided low ($\sim 5''$) and high ($\sim 1''$) resolution maps, respectively. We will present those maps in separated papers for discussing individual galaxies.

We calculated the fractions of the recovered single-dish flux from our aperture synthesis observations, which are listed in table 3. We first corrected the data cube for the primary beam attenuation, and convolved with a Gaussian single-dish beam of FWHM $45''$ (comparable to that of the FCRAO survey), and took the flux at the pointing center of the FCRAO observations. The recovered fluxes were typically 80%, which recovered almost all fluxes within the field of view.

However, a few galaxies showed exceptionally low and high recovered fluxes. The recovered flux of NGC 4535 was greater than the FCRAO flux by about twice. We made careful analyses of the raw data for several times. We made UV data for C, D, C+D, and AB+C+D array configurations, which were obtained during independent observing periods (table 2). We then CLEANed them separately, but obtained about the same flux for all of the configurations. Also the r.m.s. noises of the reduced cubes and maps are comparable to those for other galaxies observed in the same periods. Hence, we conclude that the flux calibration was correct. A flux disagreement could be possible if the FCRAO flux was significantly under-estimated, and ours was about 15% over-estimated, both within the measurement errors. The recovered flux of NGC 4548 was only 16% of the FCRAO flux. This may have happened due to the larger sizes of the missing components than the maximum detectable size of our observations (subsection 2.2). Alternatively, it could have been due to very low brightness of the extended components. In fact, the FCRAO flux is as weak as 6.7 K km s^{-1} with a $45''$ beam. If the remaining 84% is extended in the $45''$ beam, the intensity for our beam ($2\farcs6 \times 2\farcs0$) would be 5.6 K km s^{-1}. For an assumed line width of about 20 km s^{-1} in our beam, the expected brightness is only 30 mK, which is much below our detection limit.

We checked for continuum sources in the galaxies by making channel maps for a wide range of velocities. The channel maps for individual galaxies are shown in Appendix. No significant continuum source was detected in the end channels in any of the observed galaxies. However, Helfer et al. (2002; private communication by the referee) reports a continuum source in NGC 4579. In order to check this, we applied deeper continuum checking for this galaxy. We CLEANED a 2 MHz × 256-channel data cube of NGC 4579, binning each 32 channels (168 km s^{-1}). No continuum source stronger than 10 mJy was found in the outermost-velocity channels ($\sim \pm 500$ km s^{-1}), where no CO line emission is expected. Thus, the source may be strongly time variable, because this galaxy nests an AGN.

Table 4. Peak CO brightness temperatures and intensities.

NGC	$T_{\rm b,peak}$ [K]	$I_{\rm CO,peak}$ [K km s^{-1}]	$I_{\rm CO,peak} \times \cos i$ [K km s^{-1}]
4569	3.54	586	266
4419	5.71	585	229
4536	5.87	575	224
4303	6.48	436	395
4535	5.17	377	275
4192	3.26	348	96
4402	4.06	224	58
4501	1.14	210	111
4548	1.46	123	98
4212	1.38	115	78
4254	3.88	110	97
4579	0.78	84	67
4654	1.15	44	27
4689	0.62	24	21

Notes. Each value contains a systematic error of about ±15%. The inclination angles from optical isophotos (table 1) are assumed.

3. The CO Atlas of Virgo Spirals

3.1. CO Intensity Maps

The Atlas of the observed Virgo galaxies are presented in figure 1. The top-left panels show optical 'looks' for a $5' \times 5'$ area taken from the STScI Digitized Sky Survey (DSS) second-generation blue images. The inserted squares show areas for the CO maps. We present total integrated intensity maps of the CO emission in the bottom-left panels. The intensity maps were obtained by using the AIPS task 'MOMNT', which integrates the intensities by velocity only when the intensity exceeds a threshold level. The threshold level was taken to be 2 to 3 times the r.m.s. noise in the data cube. Channel maps of the observed galaxies are shown in Appendix, and will be discussed in more detail in the forthcoming papers of this series on individual galaxies. The bottom-right panel shows intensity-weighted velocity fields for the $1' \times 1'$ regions (our field of view is $65''$ at FWHP at 115 GHz), and the top-right panels show position–velocity diagrams along the major axes (top-right panels), except for NGC 4254 and NGC 4402, for which $80'' \times 80''$ regions are shown. The primary-beam correction has not been applied in these maps. The intensity scales in the maps are in Kelvin of brightness temperature (rather than in Jy beam^{-1} scale directly derived from interferometer observations) for convenience to compare with single-dish observations and to convert to the molecular hydrogen column density. We measured the peak CO intensities using these maps, and list them in table 4 together with the CO peak brightness temperatures, as read from the data cubes.

Figure 2 shows CO intensity maps in the same angular and linear scales. Each box covers a $1' \times 1'$ region, which corresponds to a 4.7 kpc × 4.7 kpc region for an assumed Virgo distance of 16.1 Mpc (Ferrarese et al. 1996). Figure 3 shows velocity fields corresponding to figure 2. In figure 4 we plot CO intensity maps on the same angular scale as in the Virgo Cluster region, where each map scale has been enlarged by 50-times the real angular size.

3.2. Velocity Fields

The bottom left panels of figure 1 show intensity-weighted velocity fields for the observed $1' \times 1'$ regions, which are the same regions for the integrated-intensity maps in the bottom-right panels. For NGC 4254 and NGC 4402, the $80'' \times 80''$ regions are presented. Figure 3 shows the velocity fields in the same angular scales. The general pattern of the velocity field in figures 1 and 3 is a symmetric spider diagram, indicating a regular circular rotation of the CO disk. Slight non-circular streaming motions, such as due to spiral arms and bars, are superposed on the regular rotation. However, there are some galaxies that show strong non-circular motion; NGC 4569 has an extremely large deviation from circular rotation, indicating either high-velocity streaming or a large-amplitude warping in the central disk.

3.3. Position–Velocity (PV) diagrams

Position–velocity (PV) diagrams are shown in figure 1 (top-right). These diagrams were made by slicing the data cubes along the optical major axes with appropriate widths for individual galaxies. Most galaxies have a steeply rising rotation velocity in the central 100 to 200 pc radii. Such a sudden rise of the rotation velocity in the close vicinity of the nuclei had not been clearly detected in lower resolution observations. One of the major purposes of the present CO survey was to obtain central rotation curves to investigate possible central massive cores, which have been found in many nearby galaxies (Sofue et al. 1999a,b; Takamiya, Sofue 2000; Sofue, Rubin 2001; Sofue et al. 2001; Koda et al. 2002). In a separate paper (Sofue et al. 2003a), we describe the result of detailed analyses of the PV diagrams and derivation of accurate rotation curves by applying a new iteration method (Takamiya, Sofue 2002), and discuss the central mass distribution.

3.4. Uni-Scale Atlas of CO Intensities

In order to give an overview of the general characteristics of distributions of the molecular gas (CO intensity) in the observed galaxies, it is helpful to compare the galaxies in a unified scheme. In figure 2, we present the observed $I_{\rm CO}$ distributions on the same angular and intensity scales. The image sizes are all $1'.0 \times 1'.0$, corresponding to 4.68 kpc × 4.68 kpc for an assumed distance of 16.1 Mpc. The contours are drawn at the same levels of 5, 10, 20, 40, 80, 160 K km s^{-1} for all galaxies.

3.5. Uni-scale Atlas of Velocity Fields

Figure 3 is the same as figure 2, except for distributions of the intensity-weighted velocities. The velocity fields generally show a 'spider diagram' pattern, indicating circular rotation of the molecular disk. The rotation velocity rises rapidly in the central few hundred parsecs, which is more clearly observed in the position–velocity diagrams in figure 1. In many galaxies, the spider diagrams are more or less distorted, indicating either non-circular streaming motion or warping of the gas disk.

3.6. Sky Plot of CO Maps on the Virgo Cluster region

In figure 4 we plot the $I_{\rm CO}$ maps on the sky area of the Virgo Cluster in a similar manner to a plot of H I maps by Cayatte

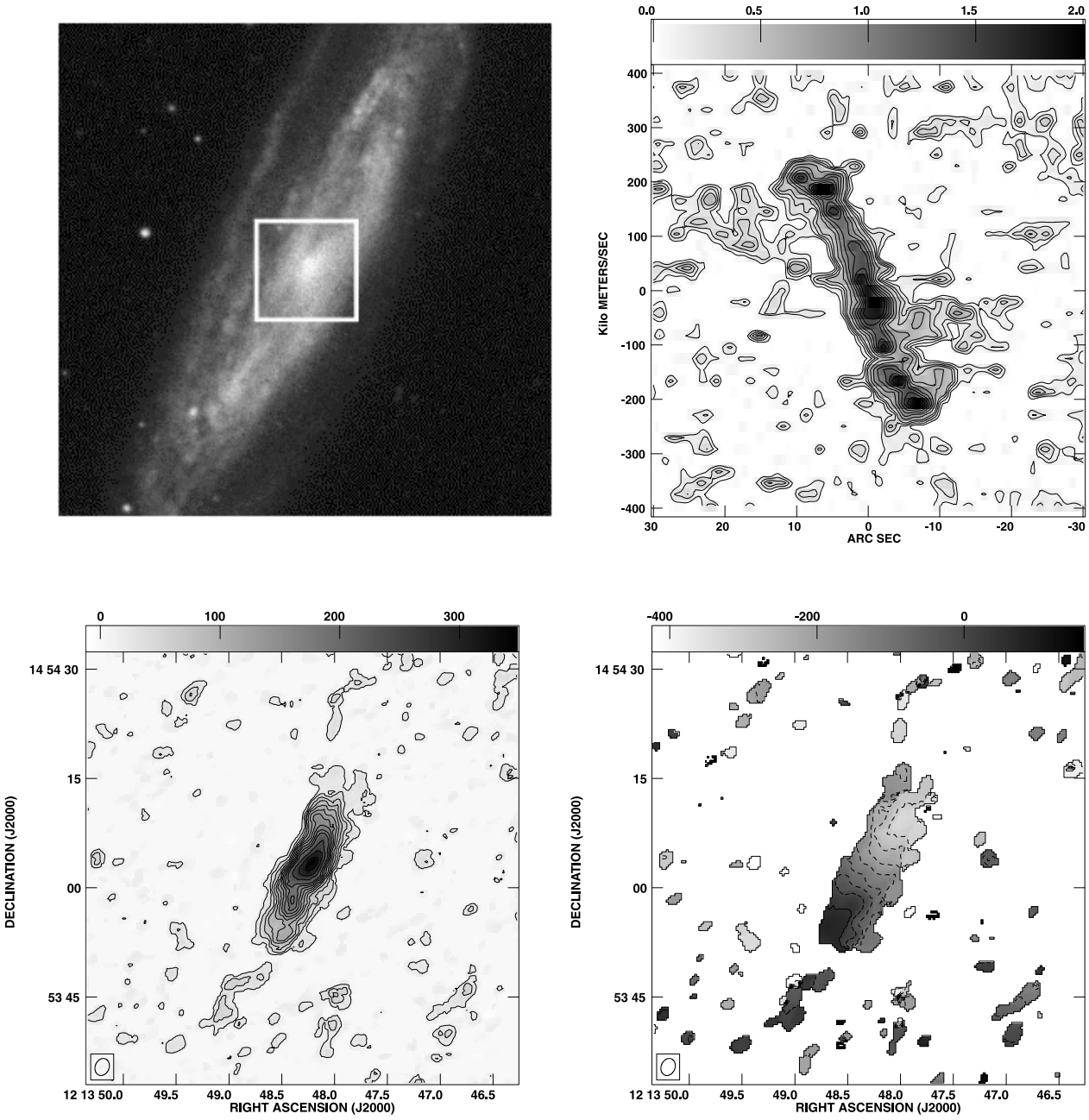

Fig. 1. Atlas of the observed Virgo galaxies. The top-left panels show DSS second-generation blue optical images, each for $5' \times 5'$ area. ^{12}CO ($J = 1$–0) observations were obtained for the central $1' \times 1'$ regions (except NGC 4254, 4402, and 4501 for $80'' \times 80''$). The bottom panels show observed CO intensity distributions (left) and the corresponding velocity fields (right). Position–velocity diagrams along the major axes are shown in the top-right panels. Parameters of the galaxies and the displayed areas are indicated in the caption for each galaxy. Indicated RA and Dec are in J2000. North is to the top, and east to the left.
(a) **NGC 4192**: (tl: top-left) DSS *b*-band $5' \times 5'$; $i = 74°$; PA = 155°. (bl: bottom-left) Ico: $1' \times 1'$; cl = $20 \times 1, 2, \ldots, 10, 12, \ldots, 16, 18\,\mathrm{K\,km\,s^{-1}}$. (tr: top-right) PVD: $1' \times 3''$, PA = 155°; cl (contour levels) = $0.1 \times (1, 2, \ldots, 10, 12, \ldots, 22)$ K. (br: bottom-right) V-field: $1' \times 1'$; cl = -400 to 50, every $50\,\mathrm{km\,s^{-1}}$.

et al. (1990). The angular scales are enlarged by a factor of 50 for individual galaxies. The CO distributions appear to be not strongly correlated with the distance from the center of the Cluster at M 87, which is marked by a cross. This property is very different from the H I gas distribution. The H I disks of the inner-cluster galaxies are usually largely distorted, and are often truncated by the ram-pressure of the intracluster medium (Cayatte et al. 1990), while the central CO disks are not strongly perturbed by the ambient gas in the cluster, probably because they lie deep in their galactic potentials.

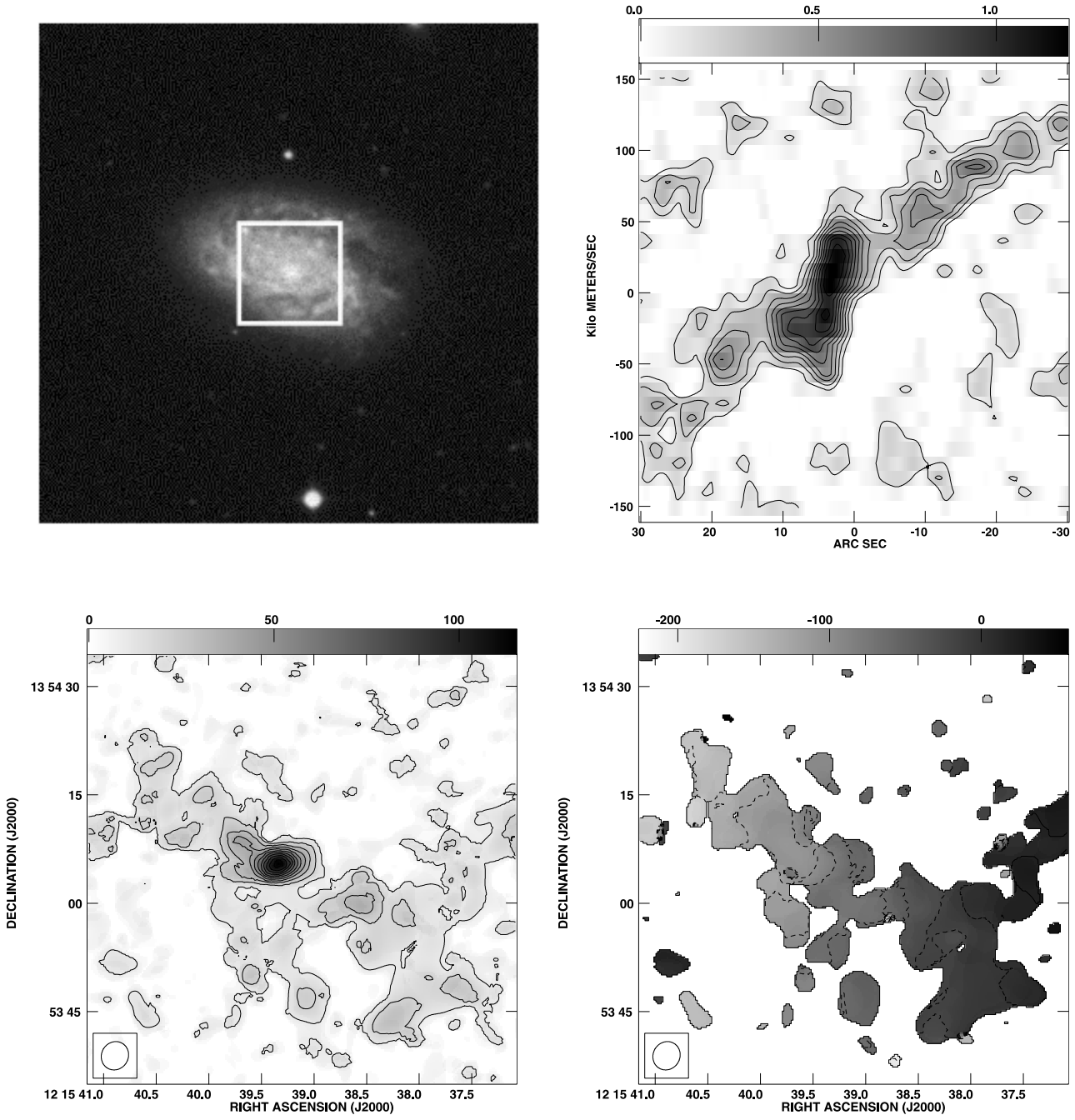

Fig. 1. (Continued.) (b) **NGC 4212**: (tl) DSS b-band $5' \times 5'$; $i = 47°$; PA = 75°. (bl) Ico: $1' \times 1'$; cl = $50 \times (0.5, 1, 2, 3, \ldots, 10)$ K km s^{-1}. (tr) PVD: $1' \times 3''$, PA = 75°; cl = $0.5 \times (0.25, 1, 2, \ldots, 10)$ K. (br) V-field: $1' \times 1'$; cl = -200 to 40, every 20 km s^{-1}.

3.7. The ViCS Data Base

The calibrated and reduced data presented in this paper will be available on our web page[1] in the form of FITS-formatted cubes and maps, and in gif-formatted images at the URL.

[1] ⟨http://www.ioa.s.u-tokyo.ac.jp/radio/virgo/⟩.

4. Central Positions and CO Distributions

4.1. Central Positions

In order to determine the central positions, we fitted a disk model with a Brandt-type rotation curve (Brandt, Sheer 1965) to intensity-weighted velocity fields using the AIPS task 'GAL'. Since this task assumes a pure circular rotation, we used only the central several arcseconds for the fitting, out of which the isovelocity contours indicate some deviations from

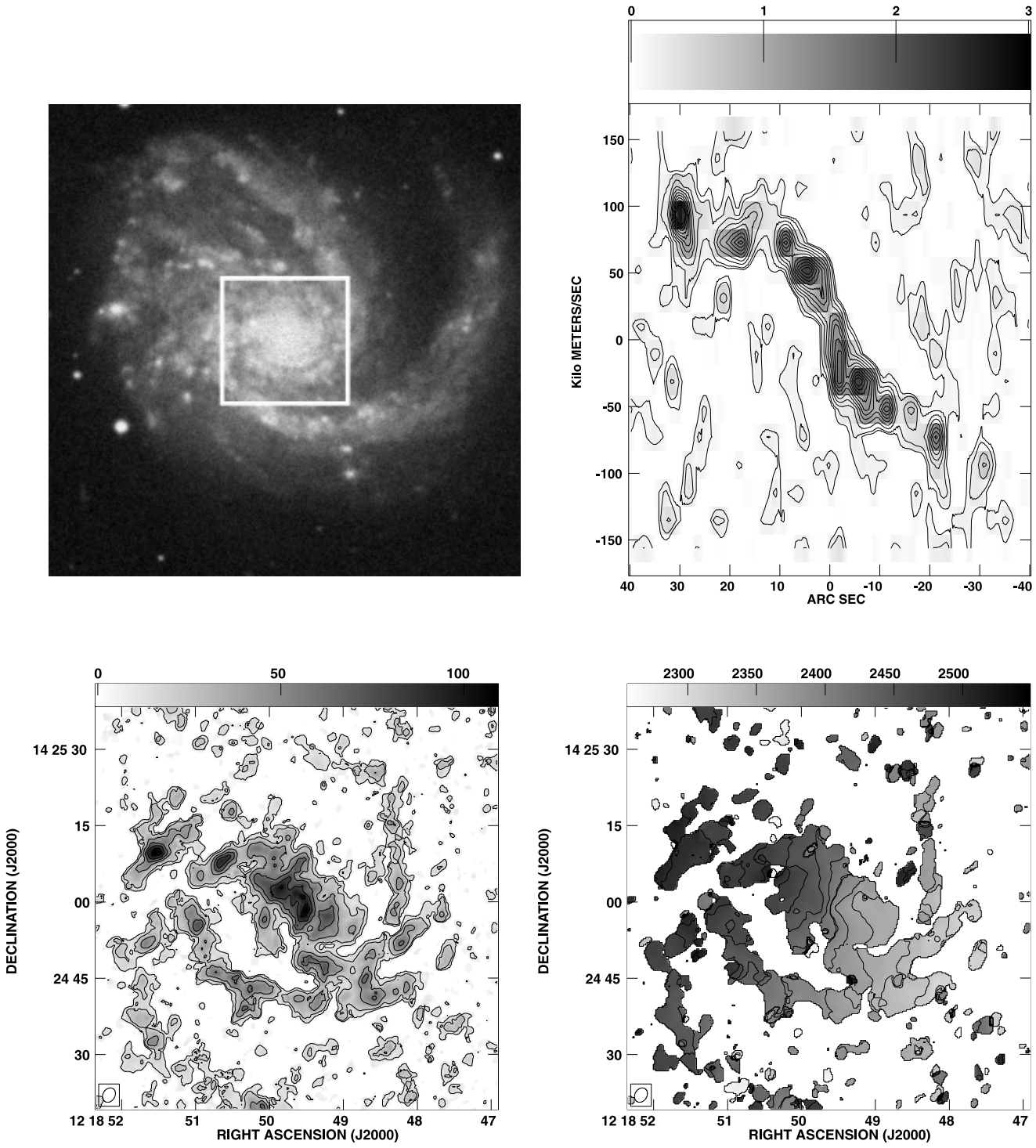

Fig. 1. (Continued.) (c) **NGC 4254**: (tl) DSS b-band $5' \times 5'$, $i = 42°$, PA = 45°. (bl) Ico: $80'' \times 80''$; cl = $10 \times (1, 2, \ldots, 12)$ K km s^{-1}. (tr) PVD: $1' \times 3''$, PA = 45°; cl = $0.132 \times (1, 2, \ldots, 12)$ K. (br) V-field: $1' \times 1'$; cl = 2300 to 2530, every 20 km s^{-1}.

circular rotation. The iteration in the task could occasionally provide different results with different initial guesses. We checked this error by changing the initial guess in appropriate ranges, and confirmed that the task suffices to provide dynamical centers accurate to about $1''$ in most cases. The derived central positions are listed in table 5.

The thus-obtained center positions were coincident with the NED center positions within an arcsecond in most cases. However, in such cases where the central CO distribution is not smooth, or the velocity field is strongly perturbed, and

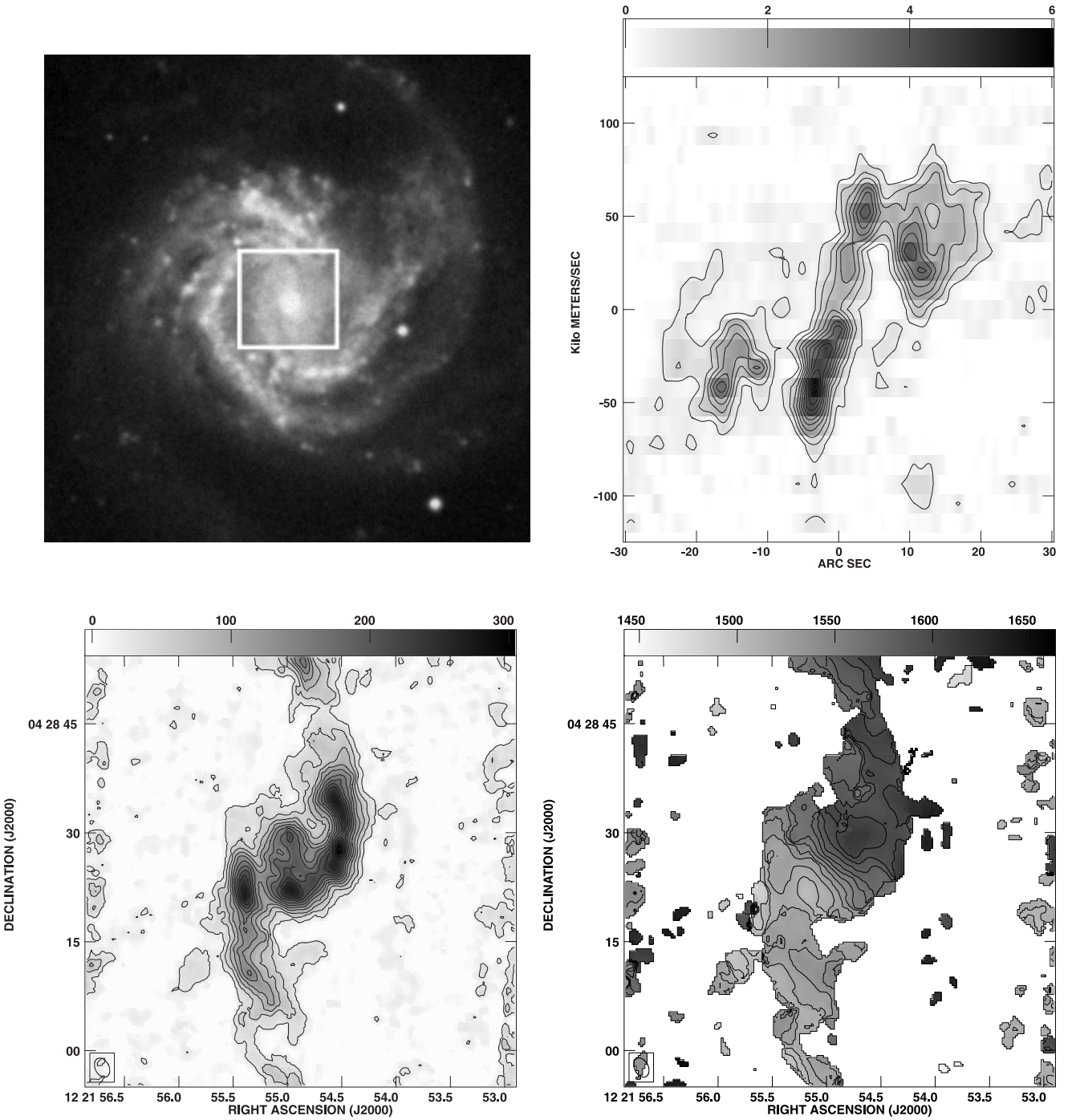

Fig. 1. (Continued.) (d) **NGC 4303**: (tl) DSS *b*-band $5' \times 5'$, $i = 25°$, PA $= 0°$. (bl) Ico: $1' \times 1'$; Beam $2\farcs80 \times 1\farcs90$; cl $= 25 \times (1, 2, \ldots, 12)$ K km s^{-1}. (tr) PVD: $1' \times 3''$, PA $= 340°$; cl $= 0.5 \times (1, 2, \ldots, 12)$ K. (br) V-field: $1' \times 1'$; cl $= 1500$ to 1600, every 10 km s^{-1}.

hence the above-mentioned dynamical centers are not reliable, we determined the central positions from the literature. The center of NGC 4212, which shows a patchy CO distribution (figure 1), was adopted from optical observations by Cotton et al. (1999), which coincides with our CO emission peak within an error of $\sim 1''$. NGC 4569 shows strong noncircular motions in the velocity field and position–velocity diagram; we adopted the central position determined by Sakamoto et al. (1999a,b) from their CO interferometry observations with a lower resolution. The center of NGC 4579 was so taken as to coincide with the position of the unresolved radio continuum source (Ho, Ulvestad 2001).

4.2. Radial Distribution of CO Gas

Figure 5 displays azimuthally averaged radial profiles of the CO-line intensities in units of K km s^{-1}, as projected on the

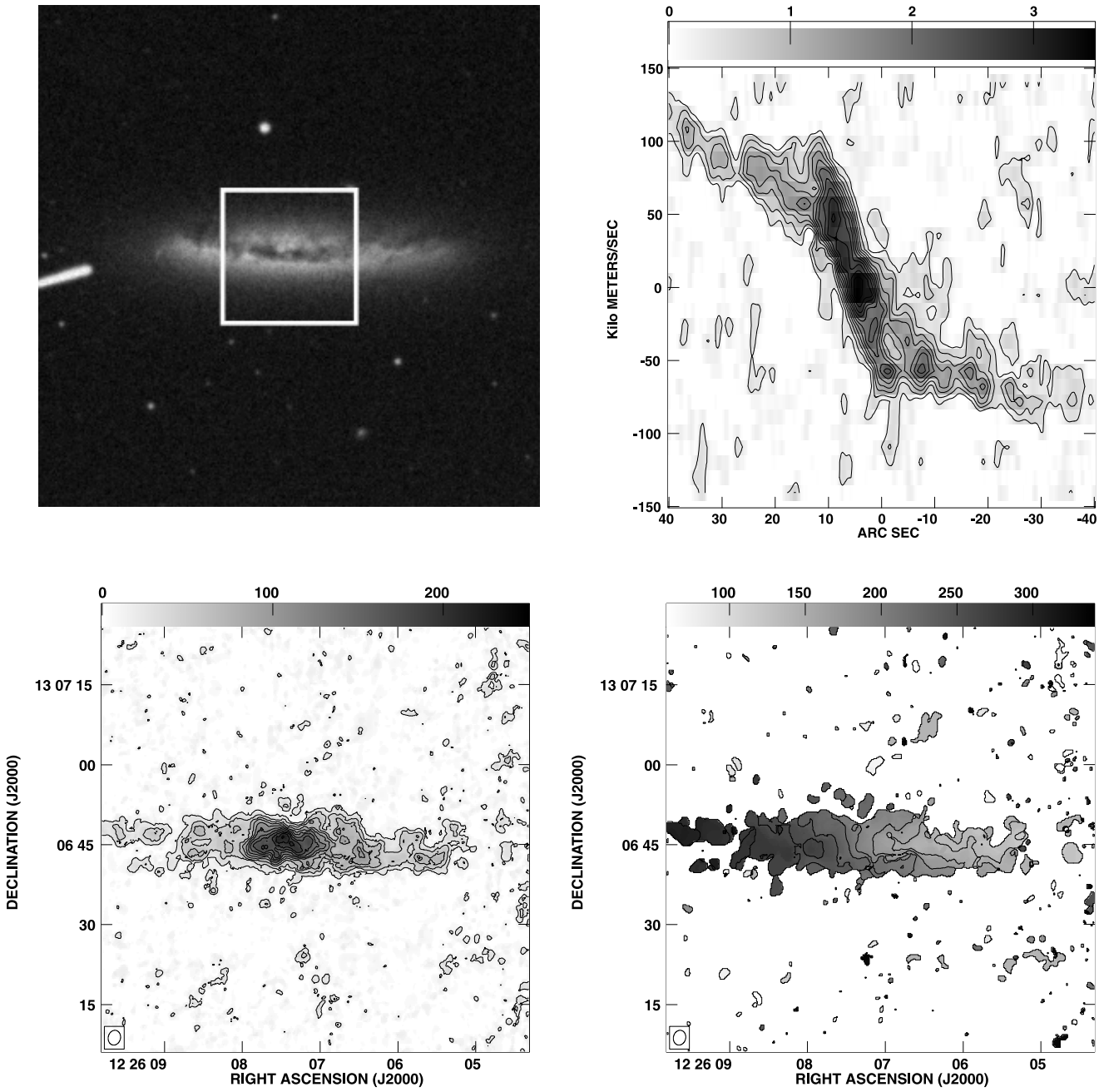

Fig. 1. (Continued.) (e) **NGC 4402**: (tl) DSS b-band $5' \times 5'$; $i = 75°$; PA = 90°. (bl) Ico: $80'' \times 80''$; cl = $20 \times (1, 2, 3, \ldots, 10)$ K km s^{-1}. (tr) PVD: $80' \times 3''$, PA = 90°; cl = $0.3 \times (1, 2, \ldots, 12)$ K. (br) V-field: $80'' \times 80''$; cl = 60 to 340, every 20 km s^{-1}.

galaxies' disks corrected for the inclinations. In order to make these plots, integrated-intensity maps without clipping were corrected for the primary beam attenuation, and we applied the AIPS task 'IRING' around the central positions derived in subsection 4.1. We fixed the inclination and position angles for each galaxy to those provided from optical observations (table 1).

The sampling intervals in the plots were set to be $0.''5$. However, the effective sampling intervals are equal to the beam widths. The number of effective sampling points for the fit increases with radius r proportionally to r, and hence the statistical error decreases proportionally to $r^{-1/2}$. The intensity error at each point in a map is given by $\Delta I = \Delta T \times N_c^{1/2} \times \Delta V$ (~ 15 K km s^{-1}), where ΔT (~ 0.3 K), N_c (~ 25), and ΔV (~ 10 km s^{-1}) are the r.m.s., number of channels within the expected velocity width, and the velocity interval, respectively, as given in table 3. Therefore, the typical error of the profiles is given approximately by $\sim 15(r/\text{beam width})^{-1/2}$ K km s^{-1}.

The intensity distributions in the central $10''$ to $15''$ regions are approximately exponential with scale radii $5''$ to $10''$, or

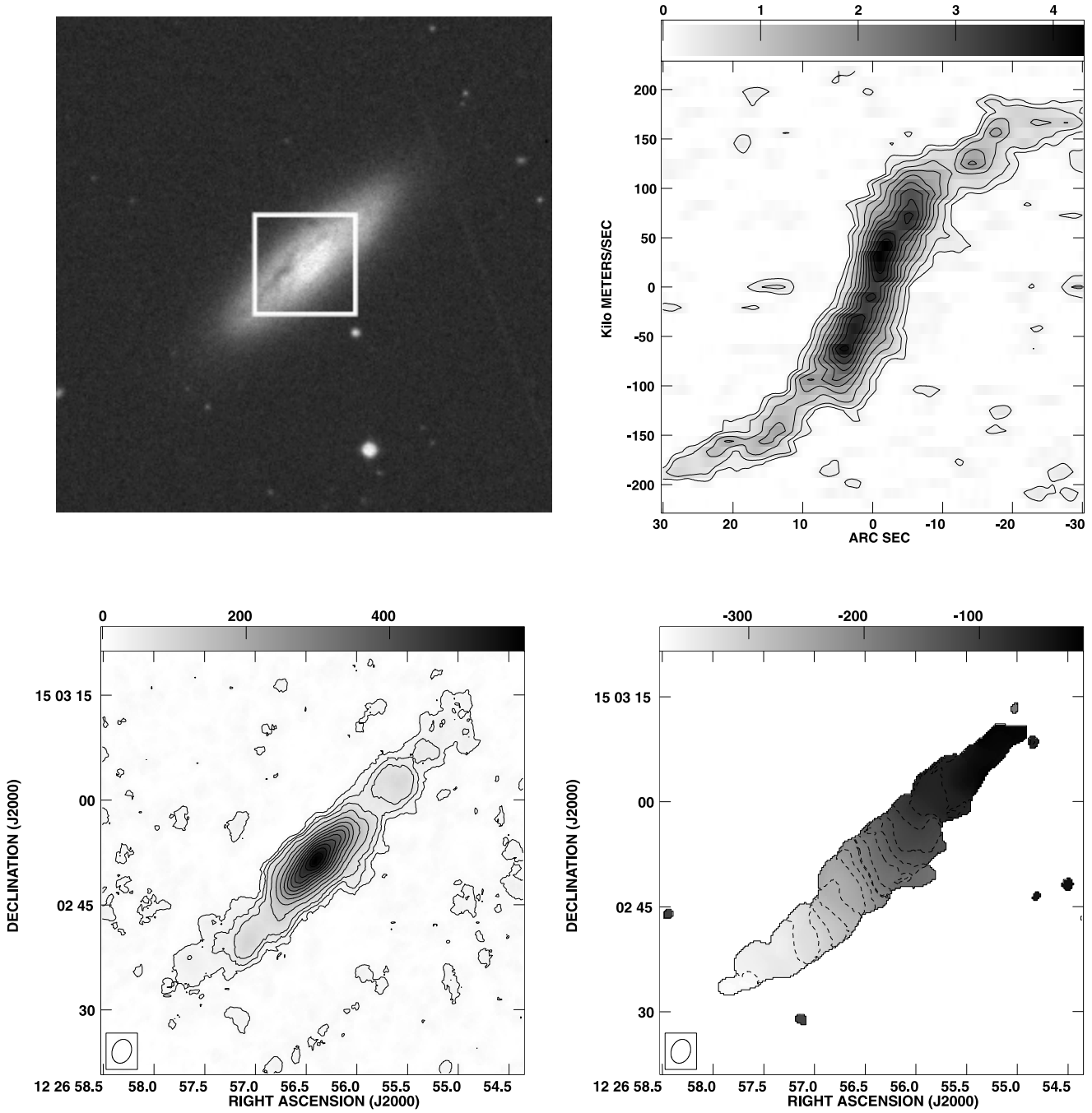

Fig. 1. (Continued.) (f) **NGC 4419**: (tl) DSS b-band $5' \times 5'$; $i = 67°$; PA = 133°. (bl) Ico: $1' \times 1'$; cl = $50 \times (0.4, 0.8, 1.2, 2, 3, \ldots, 12)$ K km s^{-1}. (tr) PVD: $1' \times 5''$, PA = 133°; cl = $0.5 \times (0.5, 1, 2, \ldots, 10)$ K. (br) V-field: $1' \times 1'$; cl = -400 to 0, every 20 km s^{-1}.

400 to 800 pc. These radii are consistent with those obtained by interferometer observations by Sakamoto et al. (1999a) for nearby galaxies at a lower resolution. Three of our target galaxies (NGC 4254, 4501, and 4569) have been observed by Sakamoto et al. (1999a), and our radial profiles are consistent with their observations. Regan et al. (2001) have noticed central components, showing bulge-like profiles, distinguished from outer disk components. The present high-resolution profiles indicate more clearly the existence of the centrally condensed component, which are distinguished from the outer exponential disk of scale radius of a few kpc, as known from single-dish observations. The scale radii of the central components are a few times smaller than those for outer extended disk components as derived from single-dish data (Sakamoto et al. 1999a) and/or BIMA + single-dish data (Regan et al. 2001).

The ellipse fit gives a quantitative presentation of the radial profiles, including the outskirts. However, the fit looses linear resolution, depending strongly on the inclination, because

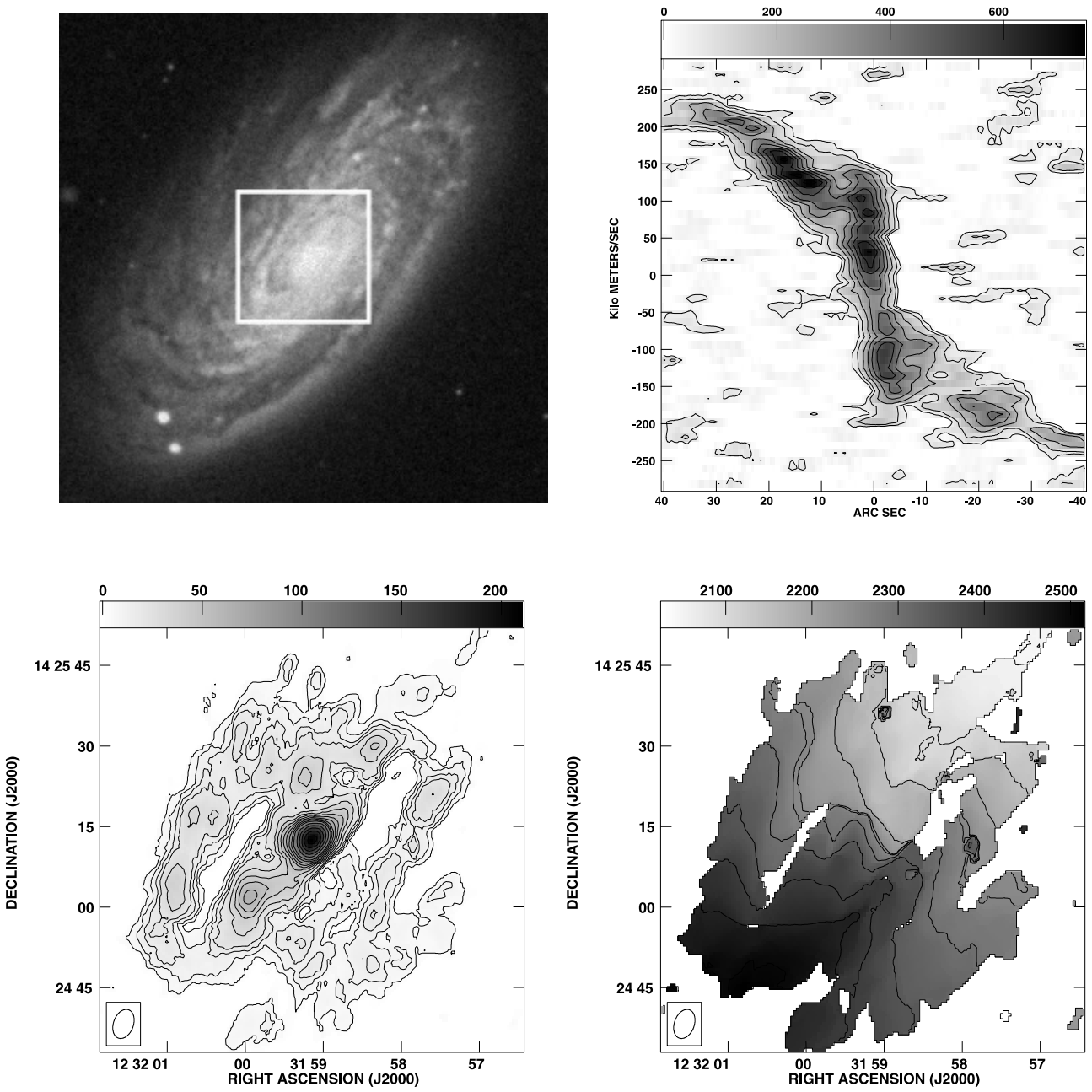

Fig. 1. (Continued.) (g) **NGC 4501**: (tl) DSS b-band $5' \times 5'$; i = 58°; PA = 140°. (bl) Ico: $80'' \times 80''$; cl = 10 × (0.5, 1.0, 1.5, 2, 3, ..., 10, 12, ..., 20) K km s^{-1}. (tr) PVD: $1' \times 10''$, PA = 140°; cl = 0.1 × (0.5, 1, 2, ..., 10) K. (br) V-field: $80'' \times 80''$; cl = 200 to 500, every 50 km s^{-1}.

it uses the data in the minor axis direction with an equal weight. Figure 5 shows that many galaxies have a strong concentration of CO gas within the central 10″ (0.8 kpc) radius, while some have a plateau or a dip at the center. We discuss such galaxies in section 5 as central-/single-peak and twin-peaks types, respectively.

5. Molecular Gas Morphology

The molecular-gas distributions show a wealth of variety. Although it is difficult to categorize them in a simple way, we can find some characteristic types in the central gas distributions. Many galaxies have a high concentration of CO gas in the central few kpc region, where the CO morphology shows either a single peak or twin peaks. More extended components have more variety of morphologies, which can be classified into arm type, bar type, and amorphous type.

5.1. Central Gas Distributions

1. Central peak and/or Single peak: Many galaxies show a strong concentration of molecular gas around the nuclei in so far as the present maps are concerned. NGC 4212,

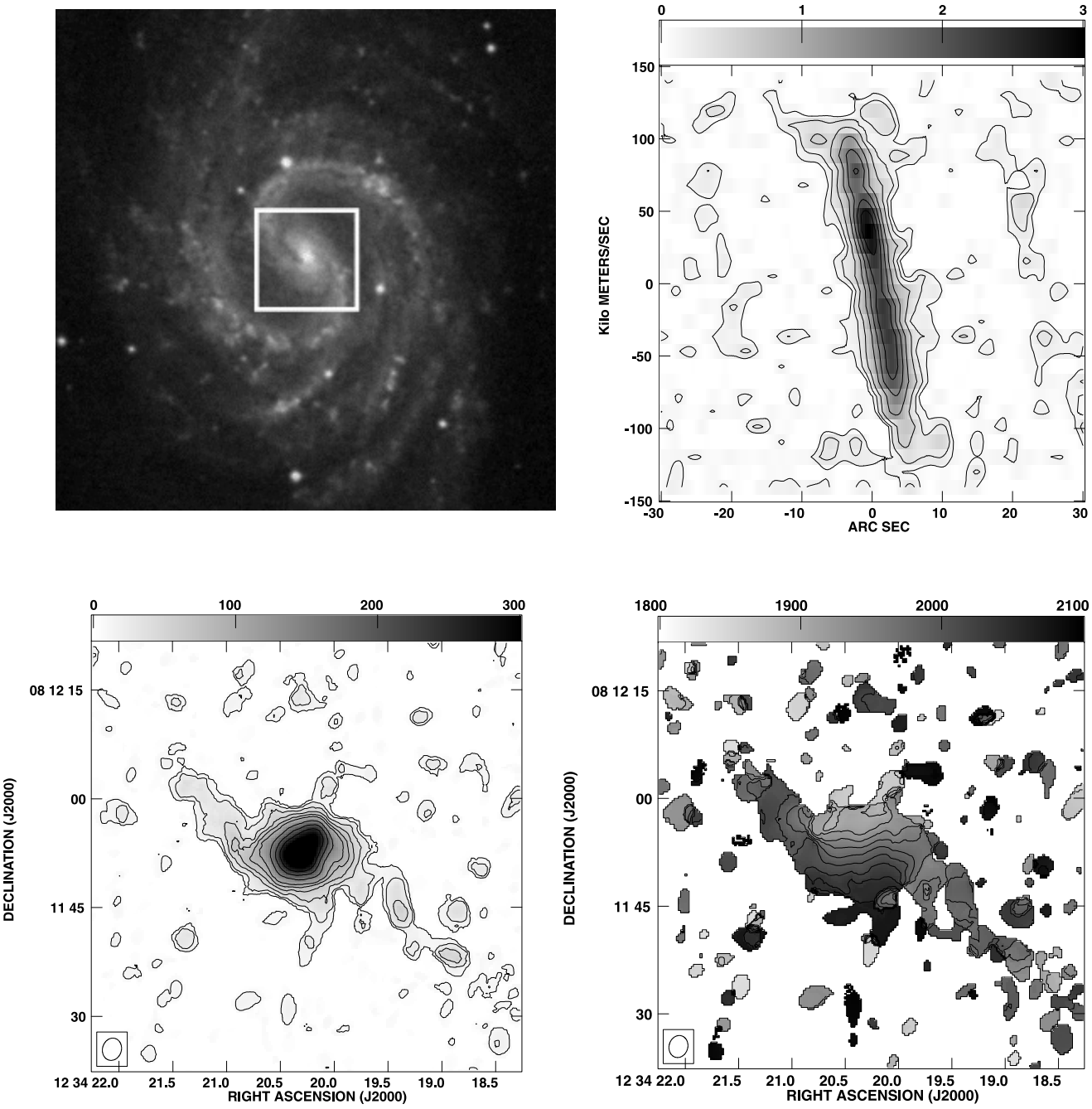

Fig. 1. (Continued.) (h) **NGC 4535**: (tl) DSS b-band $5' \times 5'$, $i = 43°$, PA = 0°. (bl) Ico: $1' \times 1'$; Beam $2\farcs80 \times 1\farcs90$; cl = $10 \times (1, 2, 4, 6, \ldots, 10, 15, 20, 25)$ K km s^{-1}. (tr) PVD: $1' \times 10''$, PA = 0°; cl = $0.5 \times (1, 2, \ldots, 12)$ K. (br) V-field: $1' \times 1'$; cl = 1800 to 2100, every 10 km s^{-1}.

NGC 4419, NGC 4501, NGC 4535, and NGC 4536 are examples. The typical size of these central peaks is about 200–400 pc. In most cases, their peaks are single at the present resolution, which we call "single peak". Figure 6 shows the CO intensity distributions in the central $20'' \times 20''$ regions (1.6 kpc square) of the central/single-peak galaxies. The central/single-peak galaxies share a considerable fraction among the observed galaxies. Note that the object selection was made by the peak antenna temperature in the FCRAO survey with a $45''$ beam. Hence, the present maps could have a selection effect for galaxies with higher peak-temperatures. However, as argued in section 2, our object selection is approximately equivalent to selection based on the CO luminosity. We may consider that the statistics with the presently observed galaxies is significant to discuss the general types of central CO morphology of the most CO luminous Virgo galaxies.

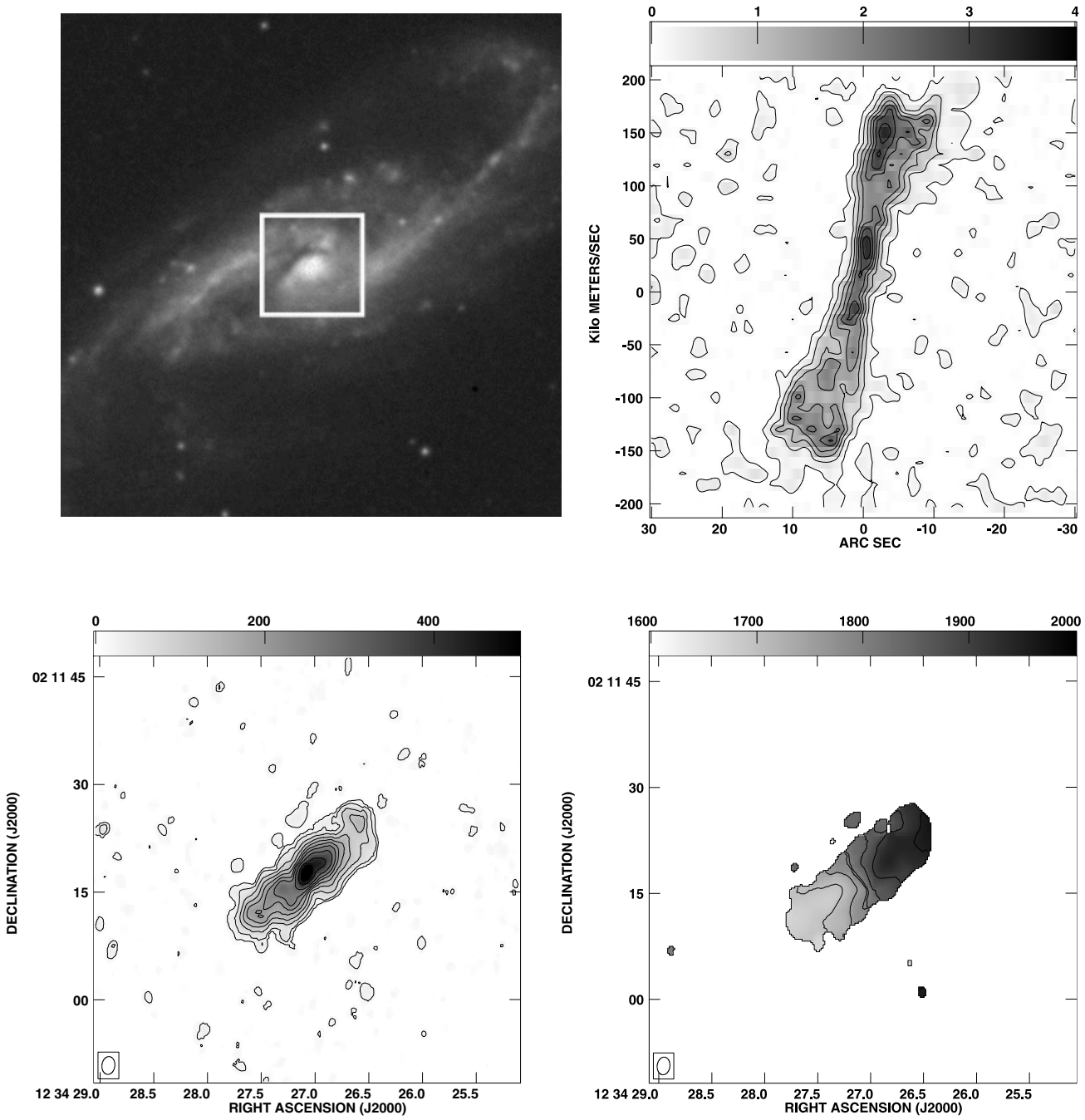

Fig. 1. (Continued.) (i) **NGC 4536**: (tl) DSS b-band $5' \times 5'$; $i = 67°$; PA = 116°. (bl) Ico: $1' \times 1'$; cl = $20 \times (1, 2, 4, 6, \ldots, 10, 15, 20, 25, 30)$ K km s^{-1}. (tr) PVD: $1' \times 5''$, PA = 116°; cl = $0.5 \times (0.25, 1, 2, \ldots, 10)$ K. (br) V-field: $1' \times 1'$; cl = 1600 to 2000, every 50 km s^{-1}.

2. Twin peaks: A typical example of the twin-peak molecular-gas distribution is seen for NGC 4303, which shows two offset open molecular arms along the optical bar, which end at a molecular ring with two peaks. Kenney et al. (1992) have reported both single-peak and twin-peak types. They selected four barred galaxies with strong CO and FIR emission, and showed that the barred galaxies have twin peaks in CO likely to be the consequence of bar-induced inflow. In so far as the present data set is concerned, which includes galaxies of random types with the CO emission concentrated in the central $45''$ (3.5 kpc) regions, twin-peak galaxies share a rather small fraction.

Kenney et al. (1992) showed that the separations between twin peaks are about 200–400 pc, while our single-peak galaxies do not have double peaks, even on the same scale ($3'' \sim 200$ pc). Note, however, that this classification may depend on

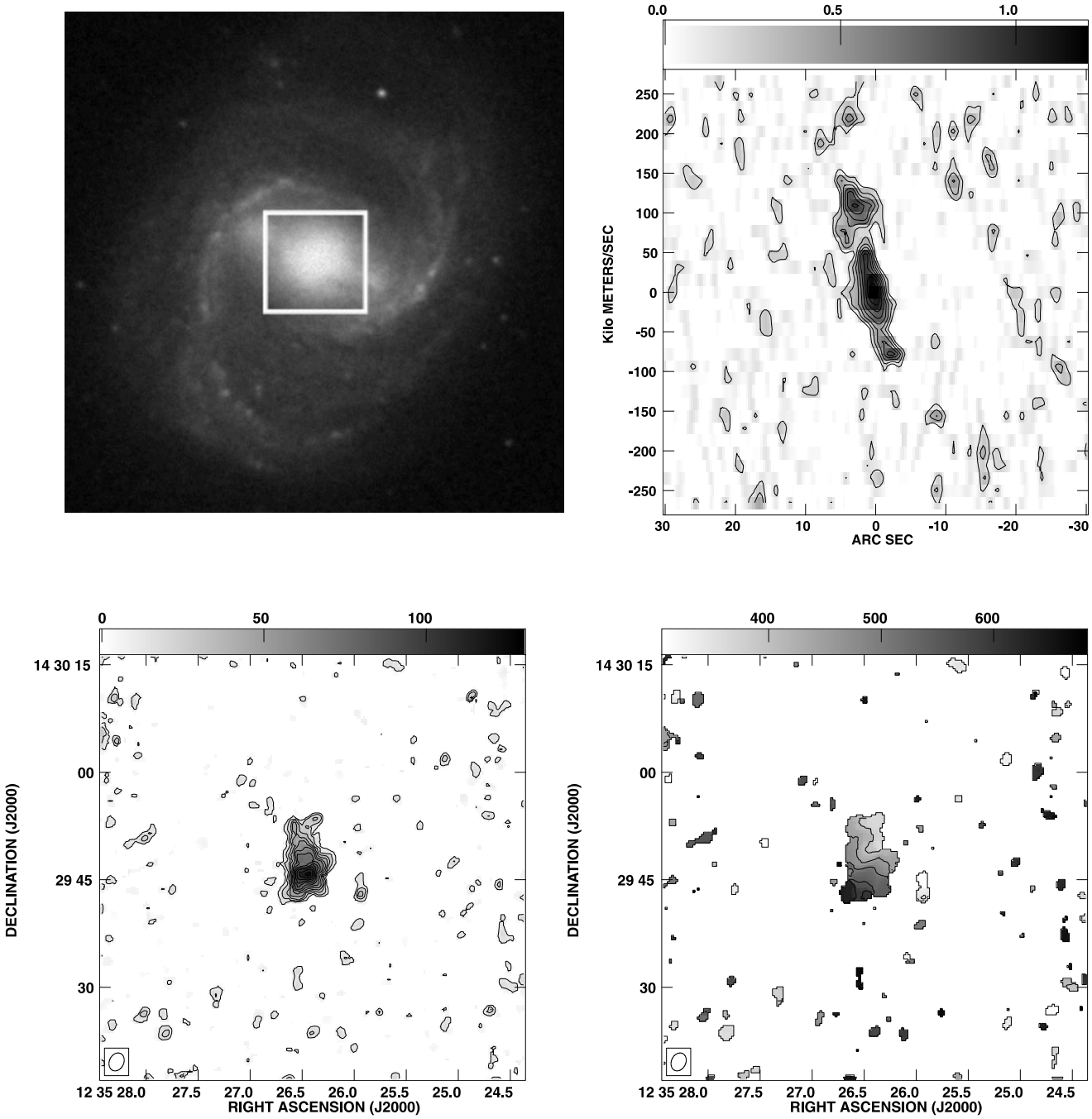

Fig. 1. (Continued.) (j) **NGC 4548**: (tl) DSS b-band $5' \times 5'$; $i = 37°$; PA = 150°. (bl) Ico: $1' \times 1'$; cl = $10 \times (1, 2, 3, \ldots, 12)$ K km s^{-1}. (tr) PVD: $1' \times 5''$, PA = 150°; cl = $0.15 \times (1, 2, \ldots, 10)$ K. (br) V-field: $1' \times 1'$; cl = 300 to 700, every 50 km s^{-1}.

the spatial resolution; it may happen that a single peak at our resolution consists of a greater number of inner structures at higher resolution. In fact, NGC 4501 appears to be a single-peak type in the present atlas, while a higher-resolution image shows a small patchy ring with a diameter of $\sim 3''$.

PV diagrams may apparently imply spatially-unresolved double peaks with separated velocities. However, a single-peak galaxy may apparently show two peaks on a PV diagram at the positive and negative terminal velocity ends at turnover radii of central rising and outer flat rotation curves, even when the gas distribution has no spatially-separated double peaks (Sofue et al. 1999a,b; Sakamoto et al. 1999a). Hence, PV diagrams may not be used for the spatial morphological classification.

6. Description of Individual Galaxies

We describe individual galaxies concerning their CO properties obtained from the present observations.

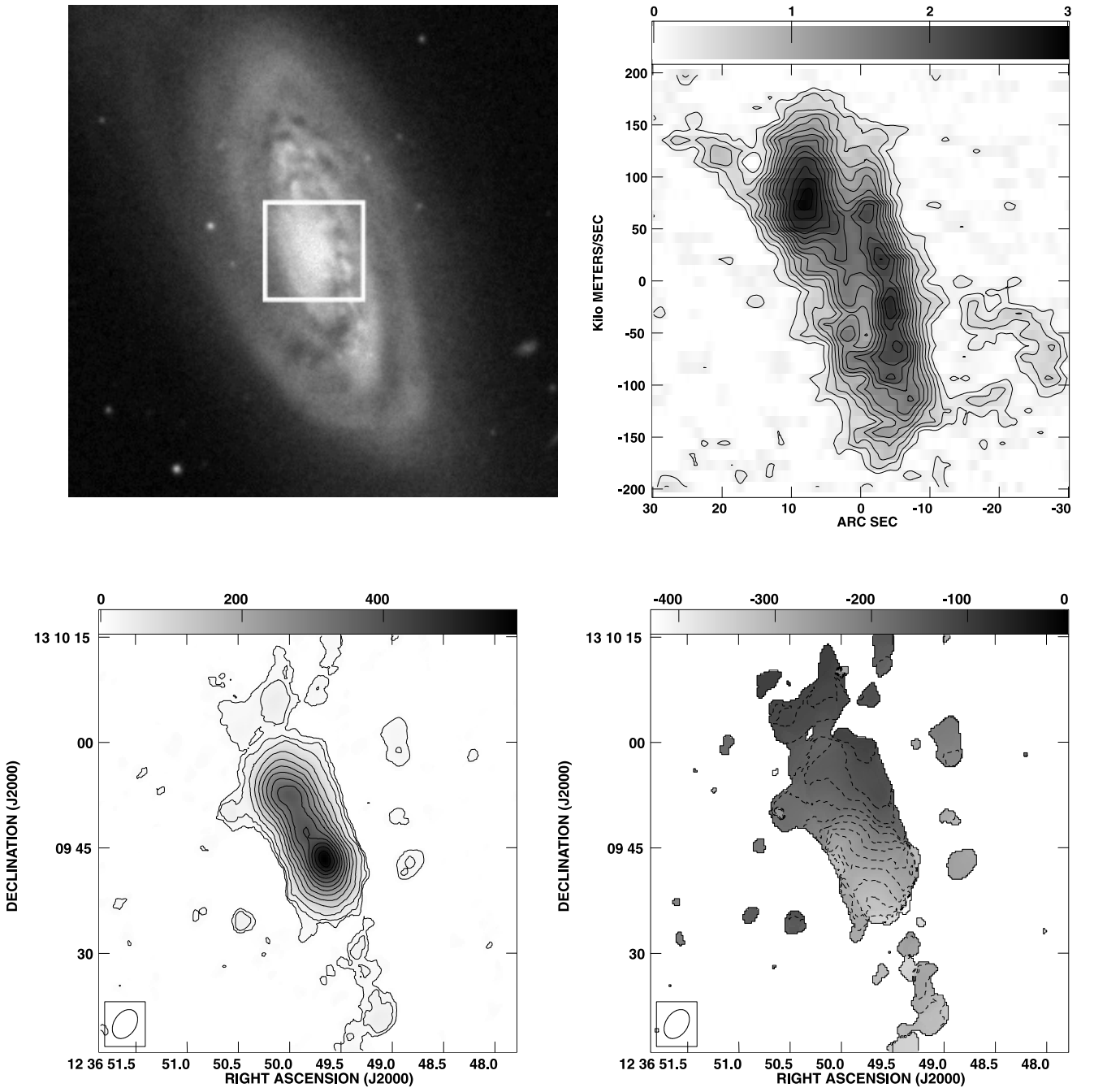

Fig. 1. (Continued.) (k) **NGC 4569**: (tl) DSS b-band $5' \times 5'$; $i = 63°$; PA = 23°. (bl) Ico: $1' \times 1'$; cl = $50 \times (0.25, 0.5, 1, 2, \ldots, 12)$ K km s^{-1}. (tr) PVD: $1' \times 5''$, PA = 160°; cl = $0.2 \times (1, 2, \ldots, 15)$ K. (br) V-field: $1' \times 1'$; cl = -380 to 0, every 20 km s^{-1}.

6.1. NGC 4192

An extremely bright CO peak is observed at the center, which classifies this galaxy in a "central-peak" type, while it appears that the peak may be resolved into two peaks at higher resolution. Hence, the classification depends on the resolution. The central peak is surrounded by a bright disk at high inclination at about the same inclination as the optical disk. The position–velocity diagram shows a very high-velocity rotation, whose maximum reaches almost 250 km s^{-1}. However, the central CO peak is rotating more slowly at about 100 km s^{-1}.

6.2. NGC 4212

The CO distribution consists of a molecular core and extended straight arms in the direction of the major axis. The core is shifted from the map center toward the NE by a few arcseconds. The velocity field and PV diagram indicate that the rotation is rigid-body-like, while the core shows a steeper

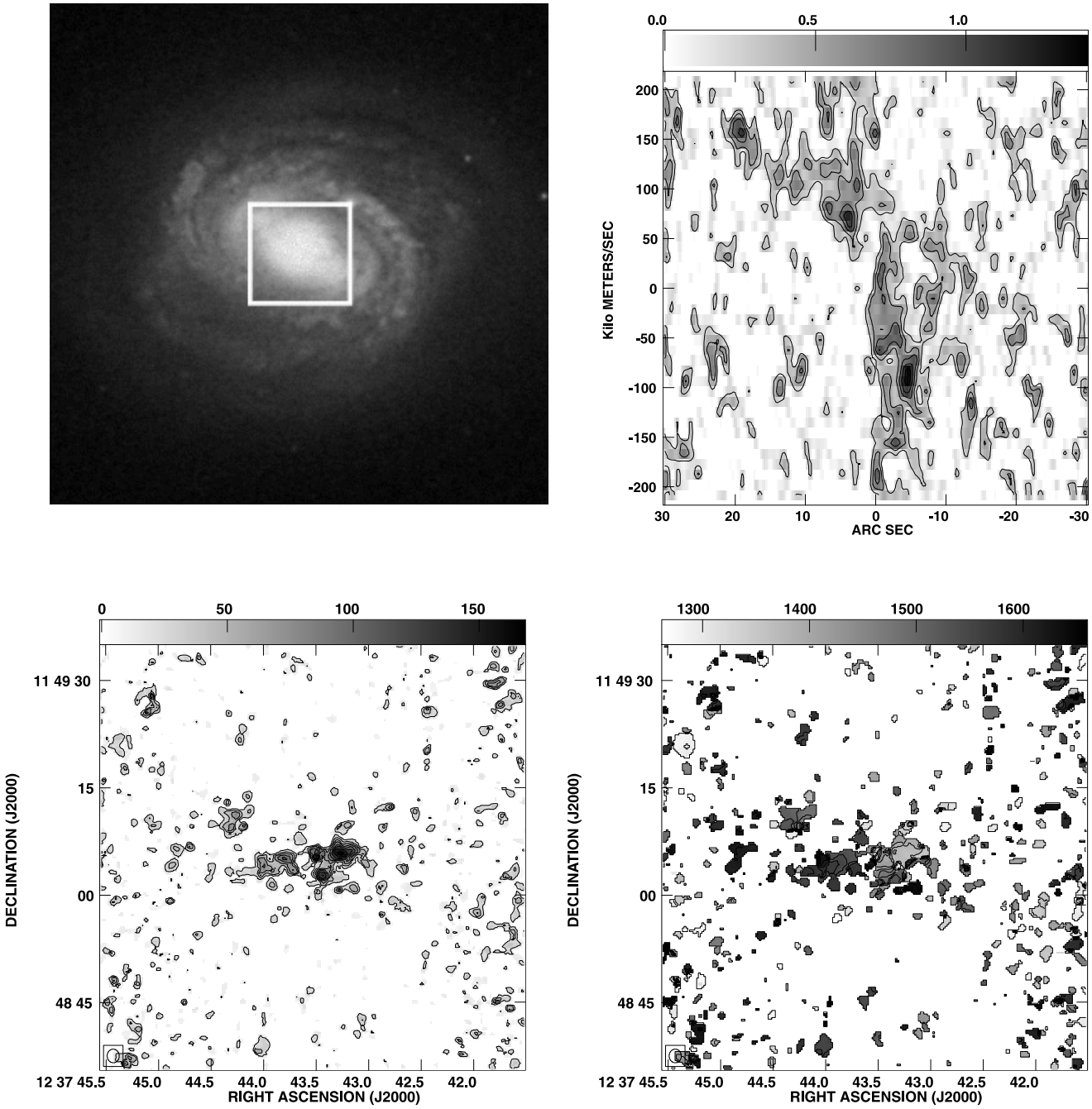

Fig. 1. (Continued.) (l) **NGC 4579**: (tl) DSS b-band $5' \times 5'$; $i = 37°$; PA = 60°. (bl) Ico: $1' \times 1'$; cl = $20 \times (1, 2, 3, \ldots, 7)$ K km s^{-1}. (tr) PVD: $1' \times 5''$, PA = 90°; cl = $0.25 \times (1, 2, \ldots, 6)$ K. (br) V-field: $1' \times 1'$; cl = 1320 to 1600, every 20 km s^{-1}.

velocity gradient.

6.3. NGC 4254

The central molecular gas distribution shows a bar-like elongation, while no optical bar feature is seen in the visual-band images. The CO intensity has a slight depression at the dynamical center, which coincides with the nucleus. Two well-developed spiral arms wind out from the bar ends toward the south and north. The south-eastern arm bifurcates into a tightly-wound dense molecular arm with an almost zero pitch angle. Hence, the molecular disk has three arms, and the arms are well correlated with the optical dark lanes. The velocity field shows a regular spider pattern, indicating a circular rotation of the disk, on which small-amplitude streaming motions due to the spiral arms are superposed. The PV diagram shows a sharp rise in the central few arcseconds, indicating a massive core, and then the velocity increases gradually. Overall, the distributions and kinematics agree with the previous

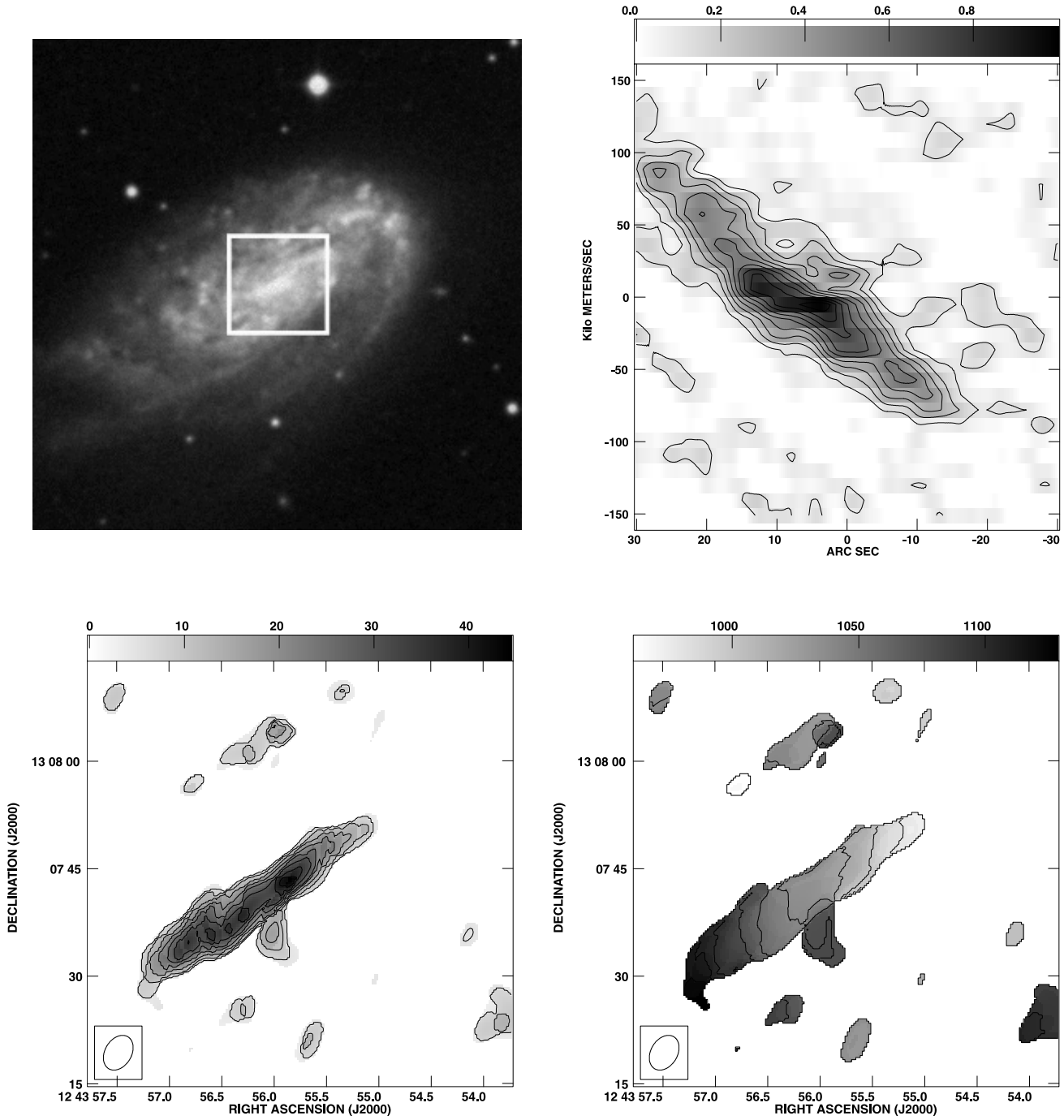

Fig. 1. (Continued.) (m) **NGC 4654**: (tl) DSS b-band $5' \times 5'$; $i = 51°$; PA = 128°. (bl) Ico: $1' \times 1'$; cl = $5 \times (1, 2, \ldots, 10)$ K km s^{-1}. (tr) PVD: $1' \times 3''$, PA = 128°; cl = $0.1 \times (1, 2, \ldots, 10)$ K. (br) V-field: $1' \times 1'$; cl = 960 to 1120, every 20 km s^{-1}.

low-resolution observations (Sakamoto et al. 1999a). A detailed study of this galaxy with consideration of the ram-pressure effect by the intra-cluster medium is presented in Sofue et al. (2003b).

6.4. NGC 4303

CO gas is highly concentrated in the nuclear disk within a radius of $r \sim 8''$ (600 pc). The nuclear disk comprises "twin peaks" at the eastern and western edges of the nuclear disk, and there appears to exist a diffuse central component around the nucleus between the twin peaks. Two prominent bisymmetric spiral arms, or offset ridges, wind out from these twin peaks, and extend toward the north and south along the dark lanes in the optical bar. The PV diagram along the major axis (north–south) indicates a rise in the rotation velocity within $r \sim 2''$ (160 pc) to 160–180 km s^{-1}. Our result is consistent with the

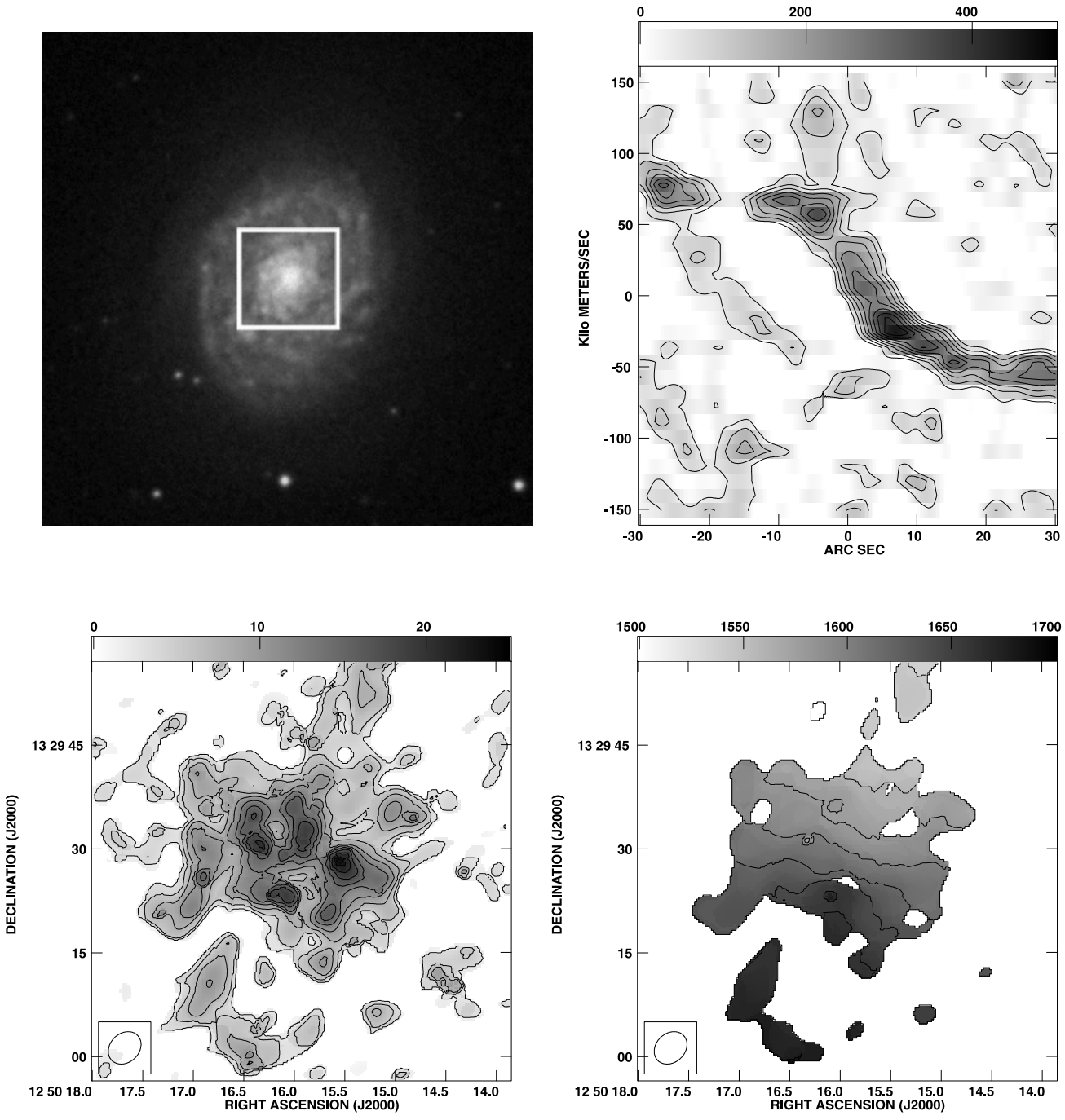

Fig. 1. (Continued.) (n) **NGC 4689**: (tl) DSS b-band $5' \times 5'$; $i = 30°$; PA = 160°. (bl) Ico: $1' \times 1'$; cl = $2.5 \times (1, 2, 3, \ldots, 10)$ K km s^{-1}. (tr) PVD: $1' \times 5''$, PA = 160°; cl = $0.05 \times (1, 2, \ldots, 10)$ K. (br) V-field: $1' \times 1'$; cl = 1500 to 1700, every 20 km s^{-1}.

high-resolution observations with the OVRO interferometer by Schinnerer et al. (2002). A detailed description of this galaxy is given in a separate paper of this series by Koda et al. (2003, in preparation).

6.5. NGC 4402

The CO intensity distribution shows a high-density nuclear molecular disk of $r \sim 10''$. The nuclear disk is surrounded by a more extended molecular disk of radius $\sim 30''$ (2 kpc). This outer disk appears to consist of two spiral arms; one extends to the west from the southern edge of the nuclear disk, tracing the dark lane, and the other arm toward the east from the north-eastern edge of the nuclear disk. The velocity field shows the usual spider diagram superposed by some streaming motion in the molecular ring/arms. The PV diagram shows a nuclear component and outer ring/arms.

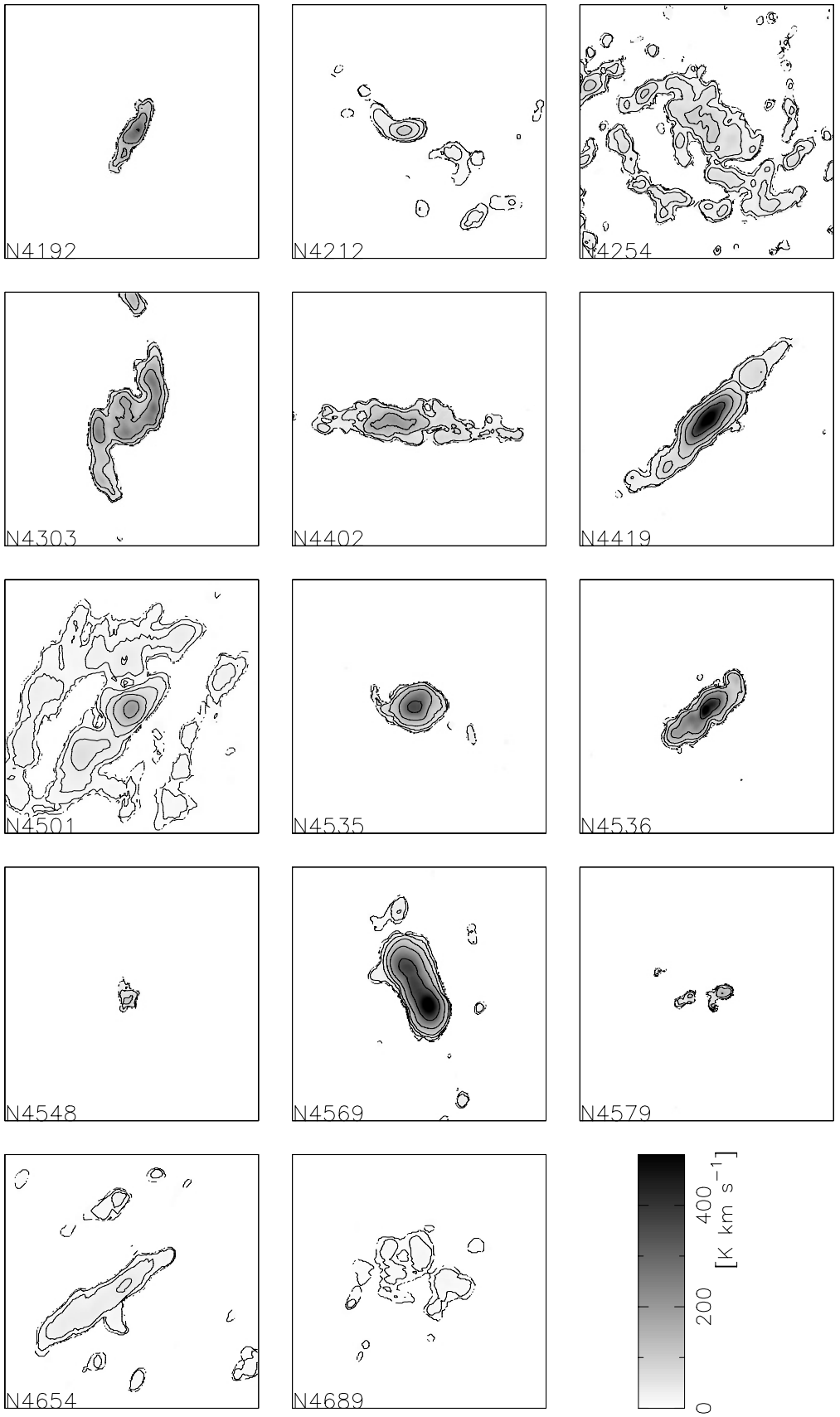

Fig. 2. Integrated ^{12}CO (J = 1–0)-intensity maps of the observed galaxies in the same angular scale. The image sizes are $1'.0 \times 1'.0$, or 4.68 kpc × 4.68 kpc for an assumed distance of 16.1 Mpc. The contours are drawn at 5, 10, 20, 40, 80, and 160 K km s^{-1}.

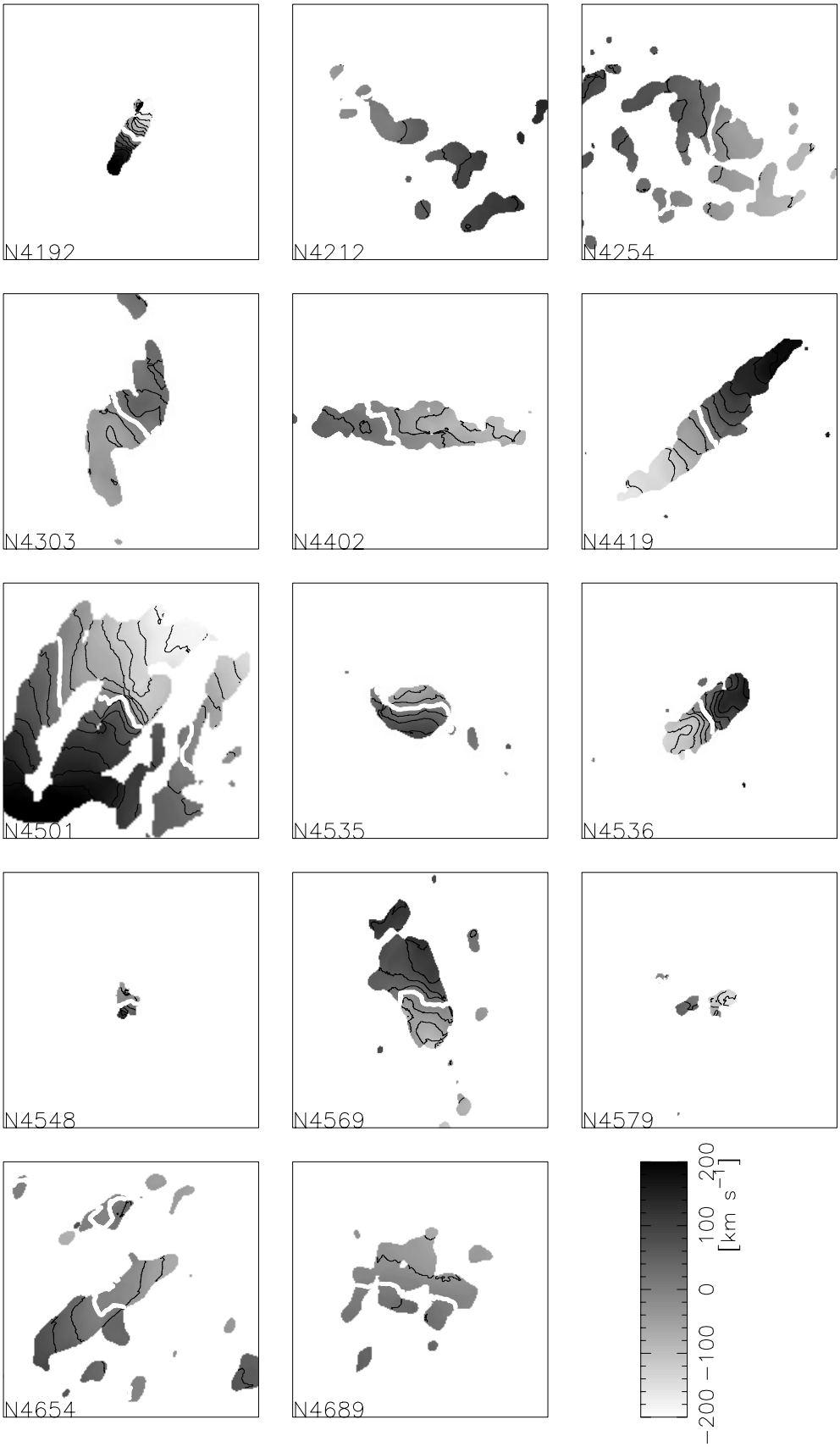

Fig. 3. CO-line velocity fields of the observed galaxies in the same angular scale corresponding to figure 2. Contours are drawn every 20 km s^{-1} relative to the systemic velocity, which is expressed by white thick contours. Darker coding represents redshift, and brighter for blueshift.

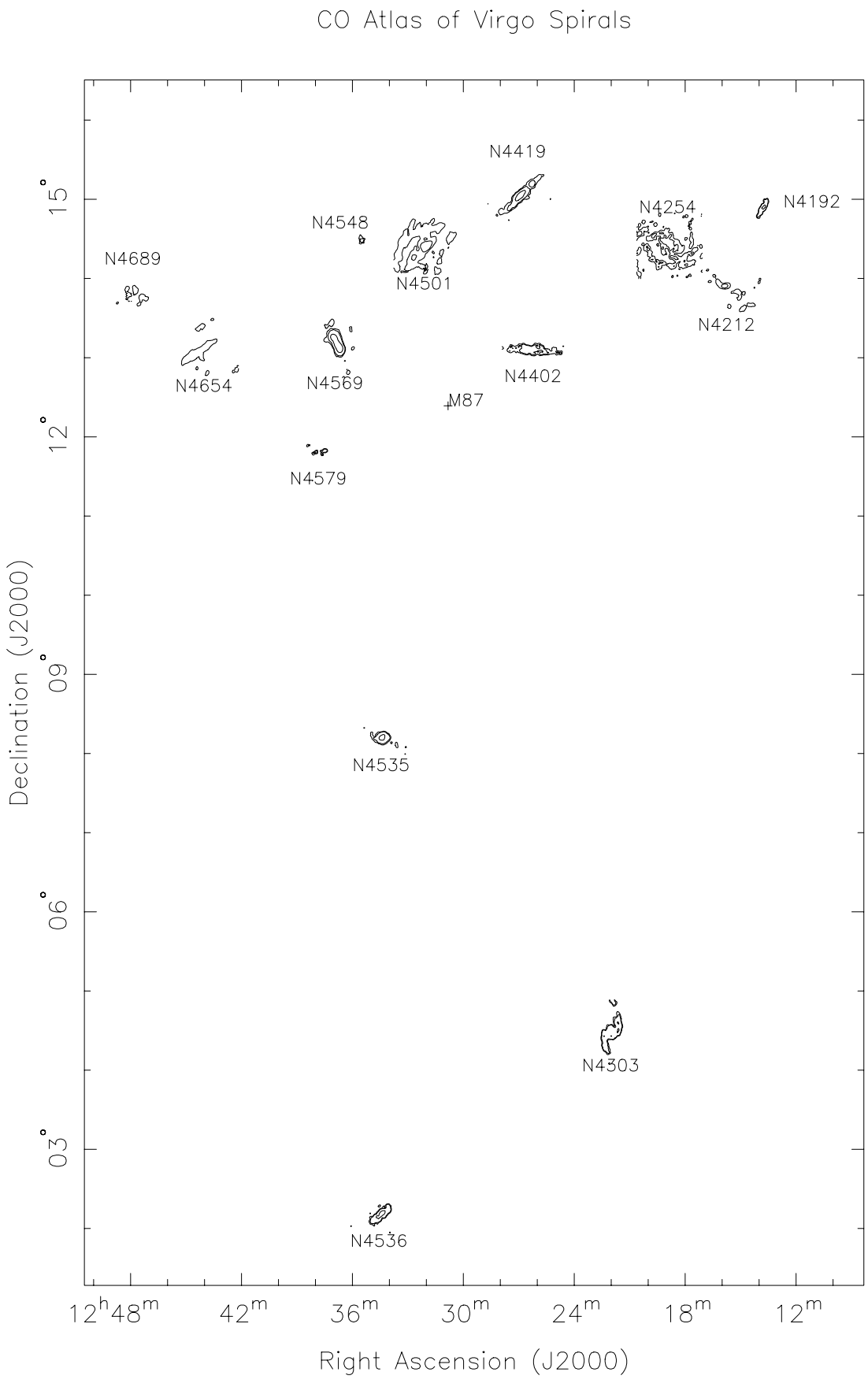

Fig. 4. Sky plot of I_{CO} on the Virgo Cluster area. Each map is enlarged by 50-times the real angular size. The position of M 87 is marked by a cross.

Table 5. Adopted parameters for analyses.

NGC	Center position (2)		Reference
(1)	RA(J2000)	DEC(J2000)	(3)
4192	12 13 48.29	+14 54 01.9	1
4212	12 15 39.40	+13 54 04.6	2
4254	12 18 49.61	+14 24 59.6	1
4303	12 21 54.94	+04 28 25.6	1
4402	12 26 07.45	+13 06 44.7	1
4419	12 26 56.40	+15 02 50.2	1
4501	12 31 59.12	+14 25 13.3	1
4535	12 34 20.35	+08 11 52.2	1
4536	12 34 27.08	+02 11 17.1	1
4548	12 35 26.44	+14 29 47.4	1
4569	12 36 49.82	+13 09 45.8	3
4579	12 37 43.53	+11 49 05.5	4
4654	12 43 56.67	+13 07 36.1	1
4689	12 50 15.86	+13 29 27.4	1

Notes. — Col. (1): Galaxy name. Col. (2): Adopted central position. Col. (3): Reference of the position: (1) This study. Dynamical center derived with the AIPS/GAL package; (2) Cotton et al. (1999); (3) Sakamoto et al. (1999a); (4) Ho and Ulvestad (2001).

6.6. NGC 4419

The CO gas is strongly concentrated in the central 5″ radius disk, which is associated with an elongated outer-disk component. Kenney et al. (1990) also reported a concentrated CO distribution. The outer molecular disk is lopsided toward the north-west. The PV diagram indicates that the central component has a rotation velocity as high as $150\,\mathrm{km\,s^{-1}}$ within 5″ radius, which is followed by a gradually rising disk rotation.

6.7. NGC 4501

A nuclear concentration of the molecular gas of radius 3″ is remarkable, as reported by Sakamoto et al. (1999a). This is classified as the "single-peak" type, although the peak intensity is not particularly high compared with the other typical single peaks. This central peak is surrounded by an extended component elongated in the SE to NW direction, with the SE end at 5″ radius being brighter. Two prominent molecular arms exist at $r \sim 20''$. The north-eastern arm is much stronger than the south-western arm. Both arms are associated with the dark lanes along the optical spiral arms. The velocity field and PV diagram indicate a sharp rise of the rotation velocity in the nuclear disk. A detailed description and modeling by spiral-shock accretion mechanism are given in Onodera et al. (2003, in preparation).

6.8. NGC 4535

The molecular gas shows a strong concentration in the central region of $\sim 6''$ radius. This galaxy is a typical "single-peak" type. Offset bars extend from the central disk toward the NE and SW, coinciding with the optical dark lanes in the bar. The velocity field shows the usual spider diagram with the zero velocity node at position angle of 90°, coinciding with the optical minor axis. However, the CO arms along the dark lanes show some non-circular streaming velocity, indicating inflow along the arms. The PV diagram shows a sharply rising, but rigid-body-like behavior within the central molecular disk.

6.9. NGC 4536

This is also a typical "single-peak" type galaxy with the molecular gas being concentrated in the nuclear disk of $\sim 10''$ radius; also, an unresolved compact core exists at the nucleus. The velocity field shows a spider diagram, and the PV diagram indicates that the rotation velocity rises to $200\,\mathrm{km\,s^{-1}}$ within the central 2″. There appears no strong non-circular streaming motion.

6.10. NGC 4548

This is a typical barred galaxy. CO emission is very weak compared with that of other galaxies. The CO distribution is highly concentrated near the nucleus, being centrally peaked, and no extended emission is detected. The recovered flux is only 16% of the FCRAO flux with 45″ beam (subsection 2.3), and the rest 84% ($5.6\,\mathrm{K\,km\,s^{-1}}$) could be due to very extended components with sizes greater than our maximum detectable size (54″).

6.11. NGC 4569

The molecular gas is highly concentrated within $\sim 1\,\mathrm{kpc}$ radius. The CO intensity distribution is elongated in the same direction as the optical major axis, and has two peaks with depression at the nucleus, consistent with the earlier CO map (Sakamoto et al. 1999a). Thus, the central molecular morphology of this galaxy may be classified in twin peaks at the present resolution. However, a higher resolution CO map reveals that the apparent two peaks coincide with both ends of an elliptical molecular ring, while they are not associated with the so-called offset ridges (Nakanishi et al. 2003). The velocity field is strongly disturbed from circular rotation, and the PV diagram indicates significant 'forbidden' velocities. Nakanishi et al. (2003) discussed the kinematics of this galaxy in detail, and tried to explain these features using two models of non-circular motion and warping of the inner disk. They conclude that it is natural that the disturbed velocity field and the forbidden velocities of the PV diagram are due to non-circular motion. Helfer et al. (2001) have reported an extended CO emission from their wide-field mosaic image. Jogee et al. (2001) have also presented a high-resolution CO image of this galaxy.

6.12. NGC 4571

No significant detection of the CO line was obtained for this galaxy, not only in channel maps, but also in an integrated-intensity map. Our resultant r.m.s. was $11.5\,\mathrm{K\,km\,s^{-1}}$ for a $130\,\mathrm{km\,s^{-1}}$ width, which is greater than $3.3\,\mathrm{K\,km\,s^{-1}}$ from single-dish observations (table 1). Since the map shows only noises, we do not present the result.

6.13. NGC 4579

The CO distribution is elongated in the east–west direction, about 30° displaced from the optical bar axis. There are two major CO peaks with asymmetric peak intensities, which

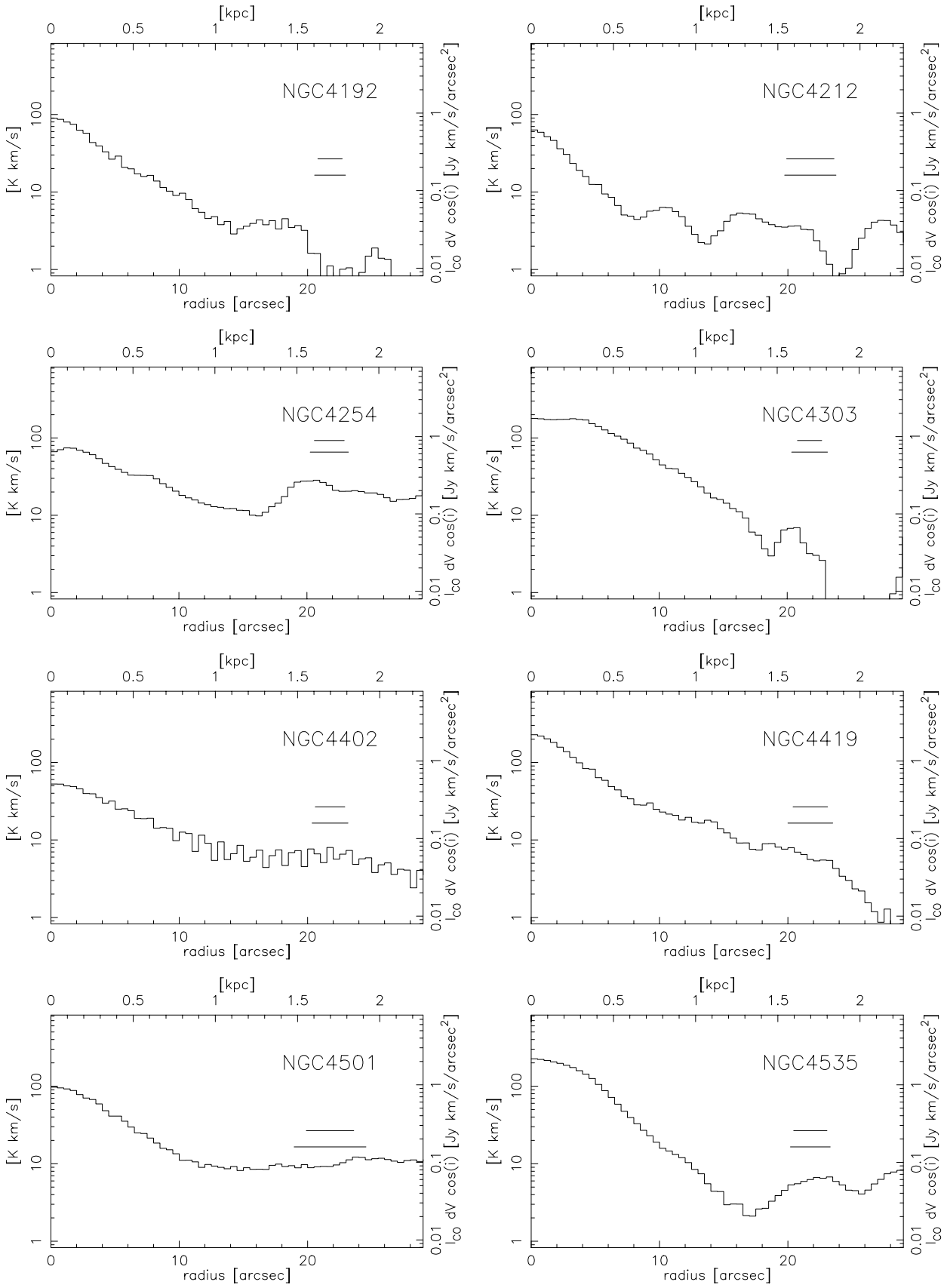

Fig. 5. Radial profiles of the face-on CO intensity obtained by ellipse fitting. The plotted radius is 30″. The primary-beam attenuation has been corrected. Two horizontal bars in each plot indicate the scales of the major and minor axes of a synthesized beam.

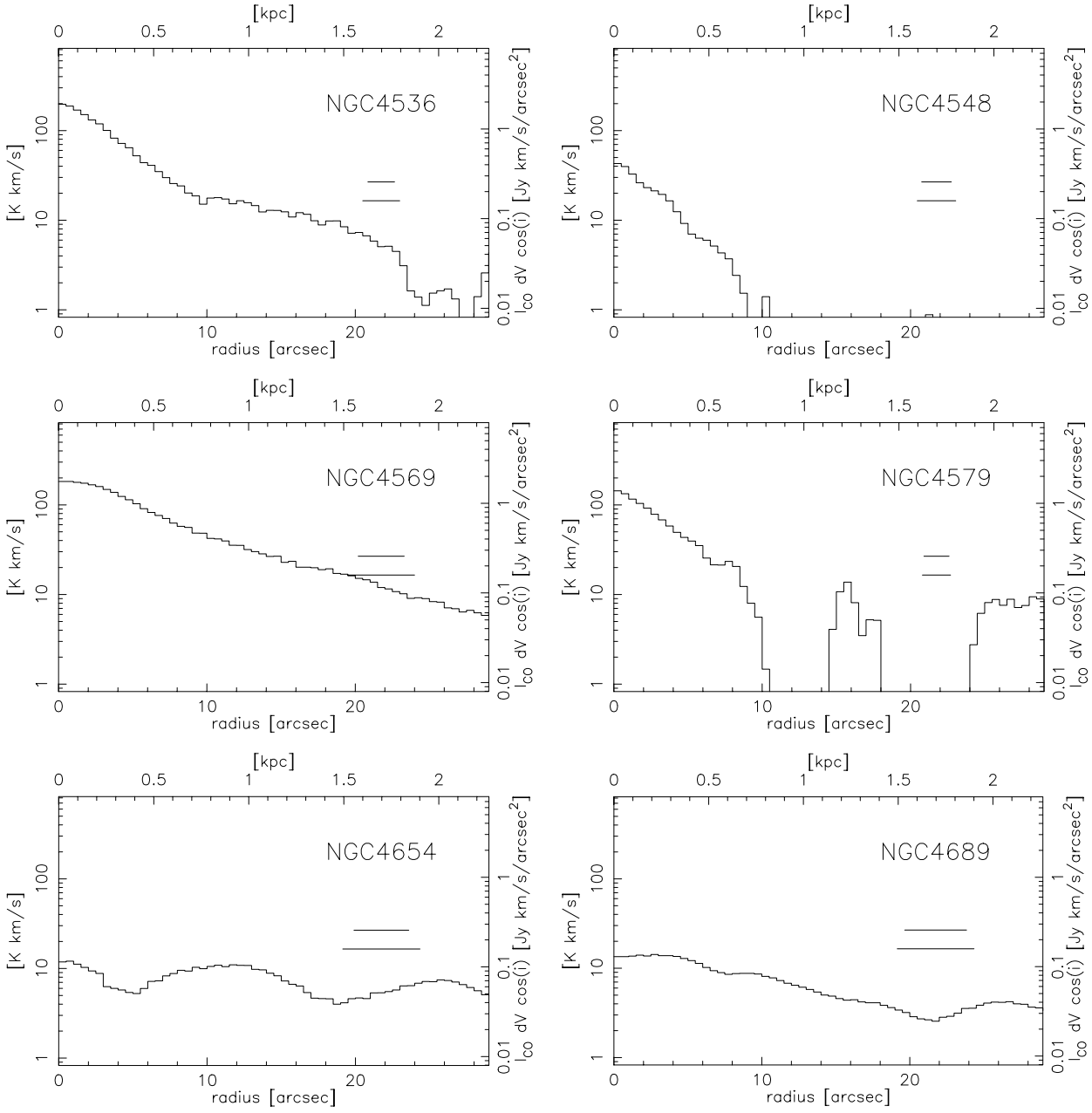

Fig. 5. (Continued.)

are associated with symmetric spiral features, as reported by Kohno et al. (1999). The velocity field shows a rotation velocity higher than 200 km s^{-1} in the central few arcseconds, which is more clearly visible in the position–velocity diagram.

6.14. NGC 4654

This galaxy is known for its lopsided structure in the optical as well as H I disks, most likely being due to the ram-pressure effect of the intracluster gas, blowing from the northwest (Phookun, Mundy 1995). The CO distribution is also lopsided, in the same direction as that of the H I and optical image tail. The lopsided CO distribution suggests that the ram-pressure effect is not negligible, even in such a central molecular disk. Moreover, the CO distribution is more elongated than the optical/H I disks. The velocity structure is rigid-body-like with a mildly increasing rotation velocity with the radius. Such rotation characteristics are exceptional among the presently observed PVDs.

6.15. NGC 4689

Like the optical spiral-arm features, the CO intensity distribution is amorphous, and is patchy and widely extended. There appear neither spiral arms nor bars in CO, and no central peaks are found. The peak I_{CO} amounts to only ~ 24 K km s^{-1}, the lowest among the observed galaxies. The velocity field indicates a regular rotation pattern, but the central rise of the

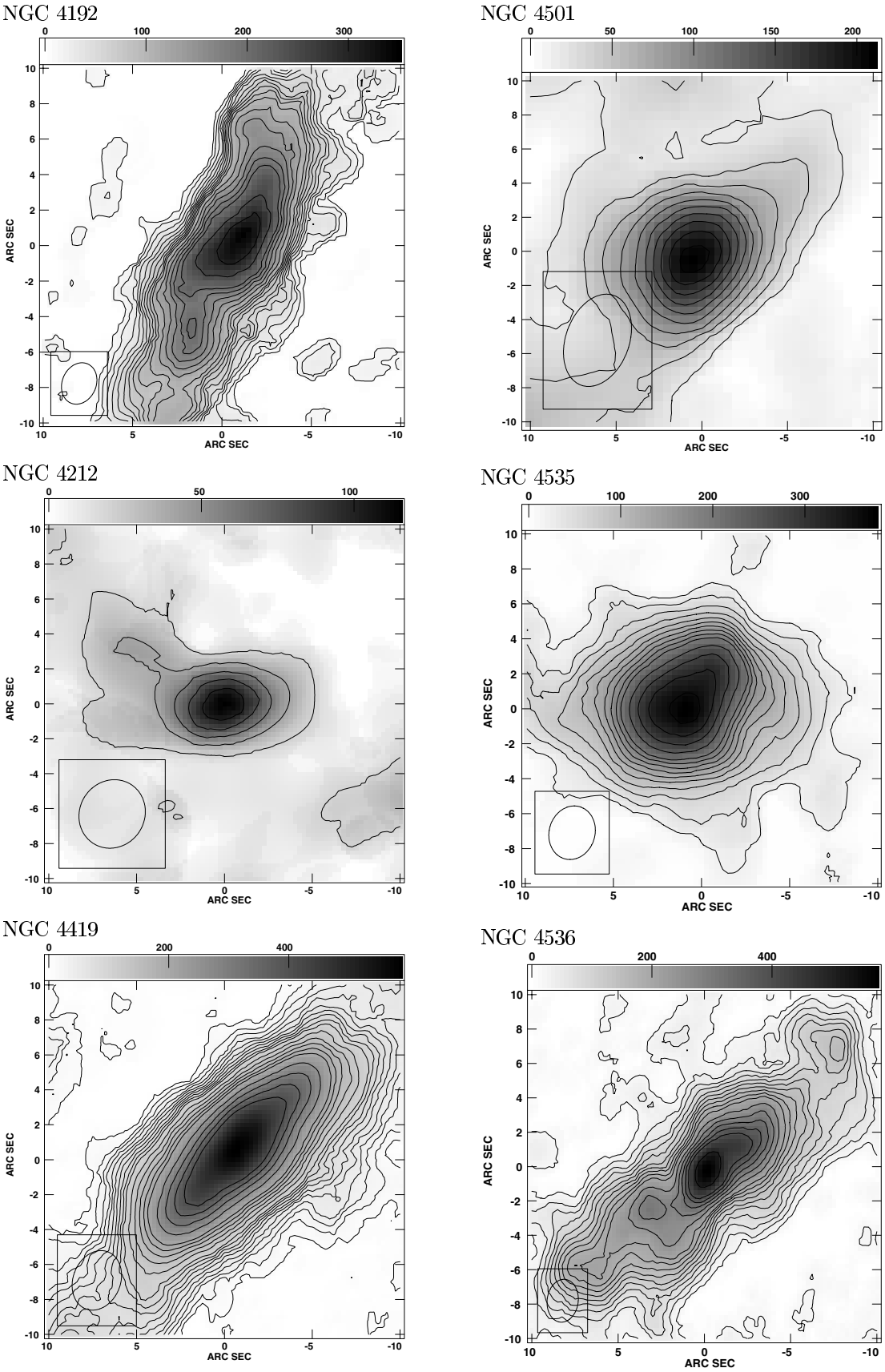

Fig. 6. CO intensity distributions in the central $20'' \times 20''$ regions of the "central/single-peak" galaxies. The contour levels are $20 \times (1, 2, \ldots, 10, 12, \ldots, 20, 25, \ldots, 40)$ K km s^{-1}.

rotation velocity is mild, as indicated by the PV diagram.

7. Summary and Discussion

We obtained a high-resolution CO-line survey of 15 Virgo spiral galaxies using the Nobeyama Millimeter-wave Array in AB, C and D configurations, and presented the result in the forms of integrated intensities, velocity fields and position–velocity diagrams along the major axes. The galaxies were sampled from the CO brightest galaxies in the Kenney and Young's (1988) list without any bias. The CO properties may be compared with each other without any ambiguity of the linear scale, because the distance to the Virgo cluster galaxies is safely taken to be 16.1 Mpc from the Cepheid calibration (Ferrarese et al. 1996). For homogeneity, our data will be useful for investigating any correlation between the CO properties and other characteristics.

We will discuss the correlation of the central-peaked CO distributions and nuclear activities in a forthcoming paper of this series. In the second paper of this series, we will derive exact rotation curves by analyzing the position–velocity diagrams, and discuss the dynamical properties of the central regions of the Virgo galaxies, as well as detailed mass distributions.

We summarize the results obtained in this paper as follows, and discuss the implications below. The mean radial profiles of the molecular gas distribution in the inner $10''$ to $15''$ radius regions are approximately exponential with an e-folding scale radius of 400 to 700 pc. In some galaxies, more extended disk components are detected, whose scale radii are greater, while the present interferometry data are not appropriate to determine the disk radii precisely.

A careful inspection of the intensity maps shows that the observed intensity distributions have a variety of types, which may be classified into the following types. The centrally-concentrated components can be classified into two types: the central-peak (or single-peak) type and the twin-peak type. The latter shows plateau-like radial profiles near the center. The distributions of more extended components can be classified into spiral arms, bars, and amorphous types. It is of particular interest to consider what causes the variety of molecular gas morphology, because it could be intimately related to the activities in the centers of galaxies.

Twin peaks of molecular gas at the ends of a set of two bisymmetric offset molecular bars (dark lanes) along the optical bar have been noticed for several barred galaxies in relation to fueling mechanisms of interstellar gas toward the central regions (Kenney et al. 1992; Sakamoto et al. 1999a). NGC 4303 is a typical case for the twin-peaks type, and the structure is well explained by a bar-potential and galactic shock hypothesis (Schinnerer et al. 2002; Koda et al. 2003, in preparation). However, the fraction of galaxies having "twin-peaks" is not particularly high in so far as the present resolution maps ($2''$–$4''$ or 150–300 pc) are concerned.

On the other hand, "central-peak" or "single-peak" galaxies share a larger fraction: five galaxies among the fifteen in the present survey at our resolution. Examples are NGC 4192 [SAB(s)ab], NGC 4419 [SB(s)a], NGC 4501 [SA(rs)b], NGC 4535 [SAB(s)c], and NGC 4536 [SAB(rs)bc].

Twin-peaks are often thought to be a consequence of characteristic gaseous orbits in a bar potential: x1 and x2-orbits in a bar intersect each other at the inner ILR, causing collision of the gas at the two intersecting points, and consequently producing twin peaks. Although this simple interpretation of the twin-peaks is attractive, the current study has shown that the single-peak is more popular than the twin-peaks. It is an interesting subject to consider the origin of the single-peak, while we need a more careful simulation and gas dynamics. We here try to speculate a possible mechanism.

First of all, the twin-peaks are not the final and stable structure of the gas distribution in a bar. The self-gravity of the gas will cause a collapse in the gas structures, particularly such large clumps as twin-peaks will be gravitationally unstable, and cause a further infall of gas into the center due to the friction among the clouds (Wada, Habe 1992). Moreover, if there exists a central massive object, the friction due to stronger shearing motion will accelerate the accretion toward the nucleus (Fukuda et al. 1998). In fact, most of the galaxies show a very steep rise of rotation curve in the central ~ 100 pc region, indicating the existence of massive compact cores of mass 10^8–$10^9 M_\odot$ around the nuclei (Sofue et al. 2003a). Hence, the central single-peak may be formed after the twin-peaks have developed.

The above mechanism could work even if a galaxy shows no prominent bar in the optical/infrared photographs, because even a very weak bisymmetric distortion of a disk potential can cause non-circular motion of gas (Koda, Wada 2002). Also, Onodera et al. (2003, in preparation) discuss another possible mechanism to produce a central single-peak by stellar spiral arms for the case of NGC 4501, which indeed has no bar, but shows a continuous spiral structure from the disk to the nucleus.

The observations were performed as a long-term project from 1999 December till 2002 April at the Nobeyama Radio Observatory (NRO) of the National Astronomical Observatories of Japan. We are indebted to the staff of NRO for their help during the observations. We thank T. Takamiya and M. Hidaka for their help with the observations and reductions, A. Kawamura and M. Honma for their help with the observations. The data reductions were made using the NRAO AIPS package. We made use of the data archive from NASA Extragalactic Database (NED). J. K. was financially supported by the Japan Society for the Promotion of Science (JSPS) for Young Scientists.

Appendix.

We show the channel maps of individual galaxies in figure A1.

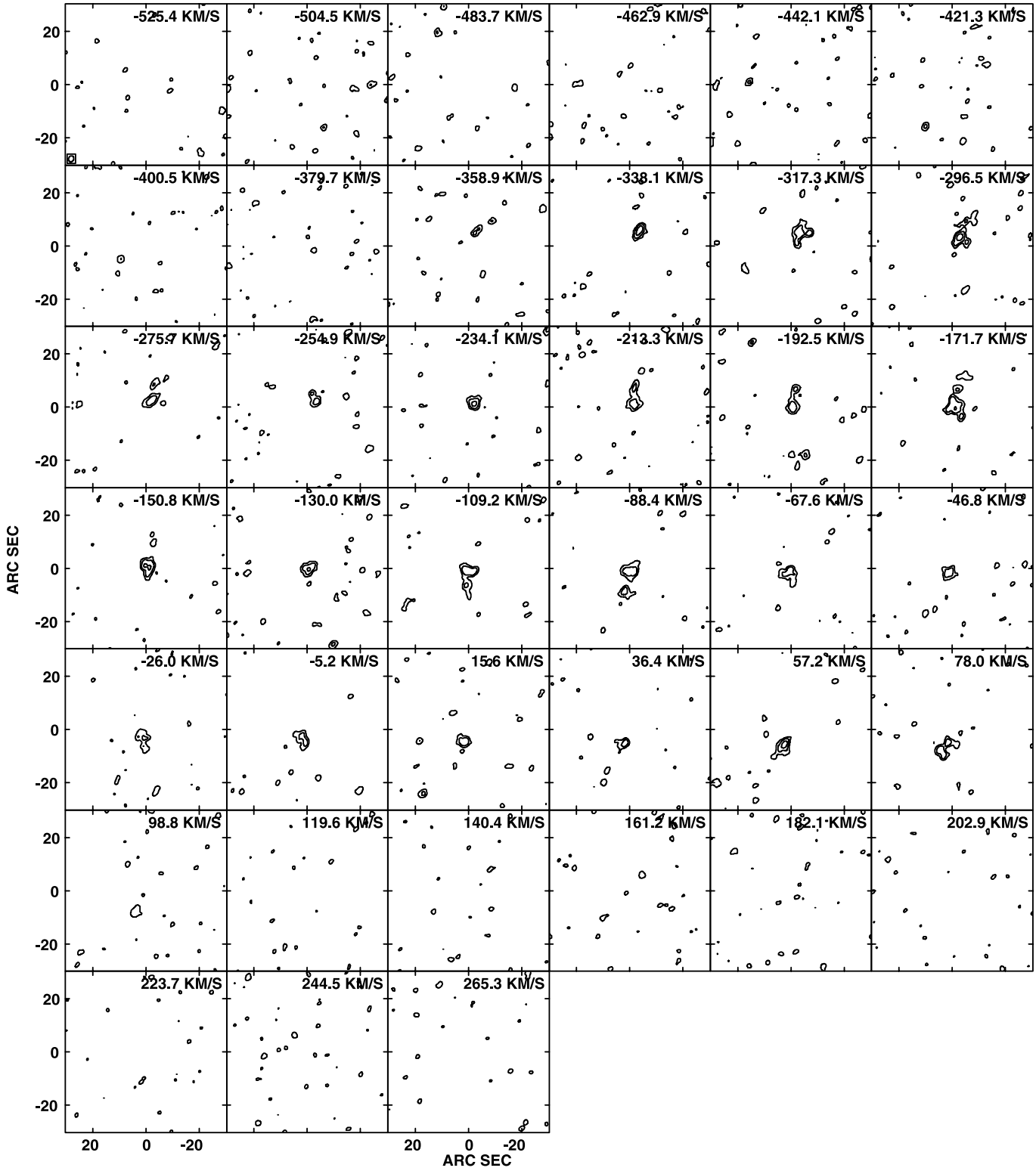

Fig. A1. Channel maps of the ^{12}CO (J = 1–0) line emission of the Virgo galaxies. Intensity scale is in Kelvin of brightness temperature. Contours are drawn at 2^n times the lowest-contour value ($n = 1, 2, 3, \ldots$). The lowest contour level (cl) is indicated for individual galaxies.
NGC 4192: Lowest cl (contour level) = 0.5 K.

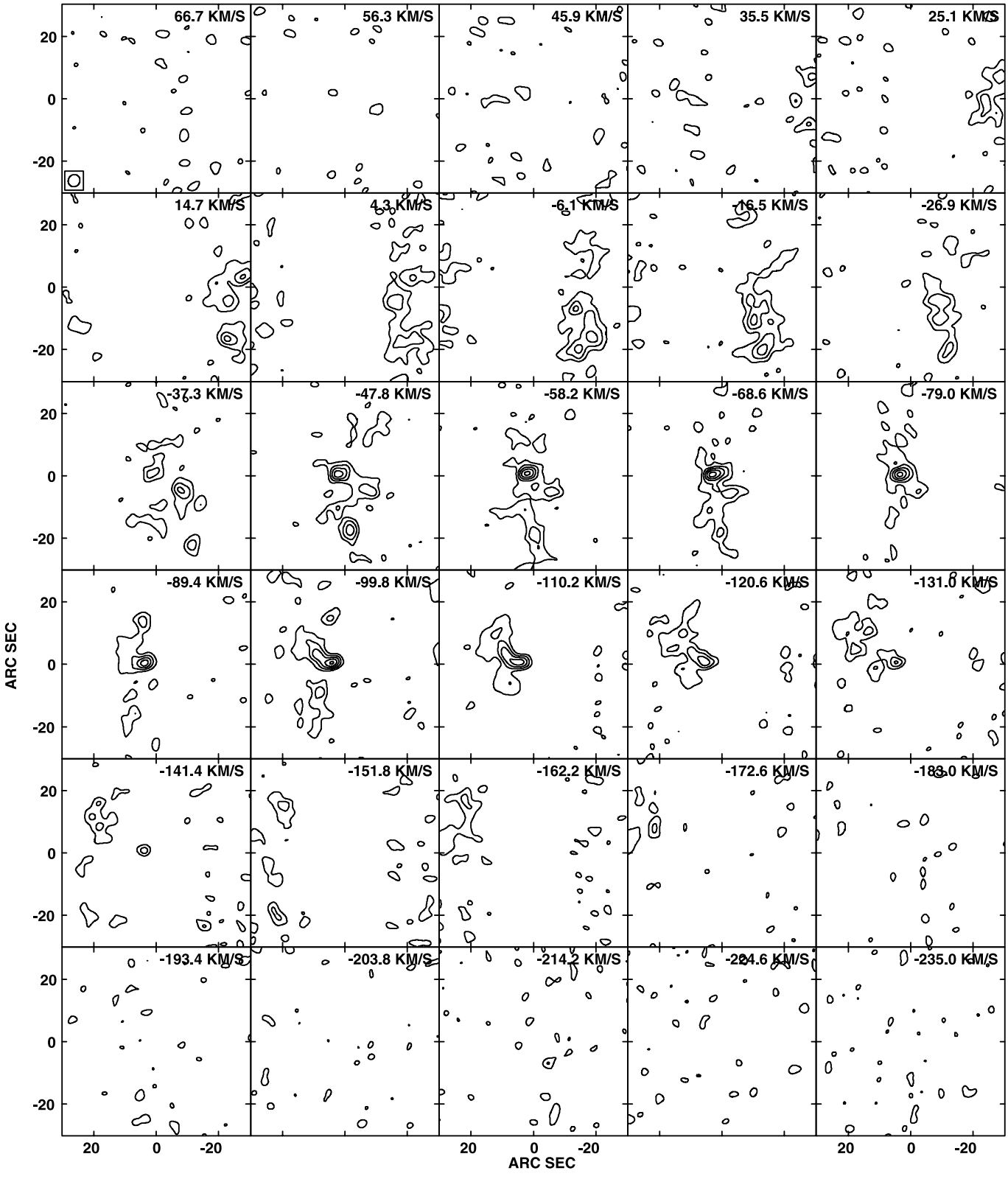

Fig. A1. (Continued.) NGC 4212: Lowest cl = 0.25 K.

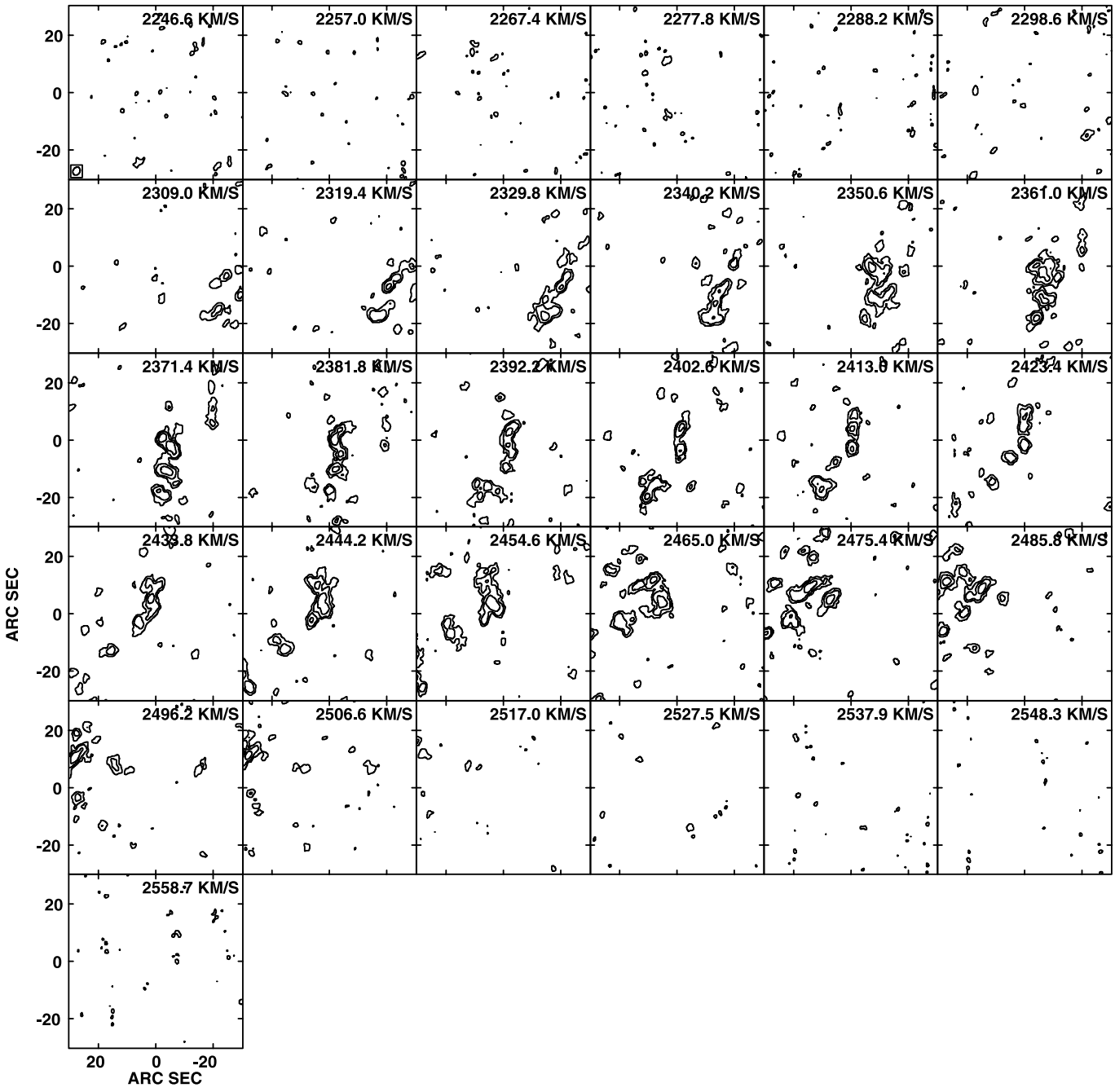

Fig. A1. (Continued.) NGC 4254: Lowest cl = 0.5 K.

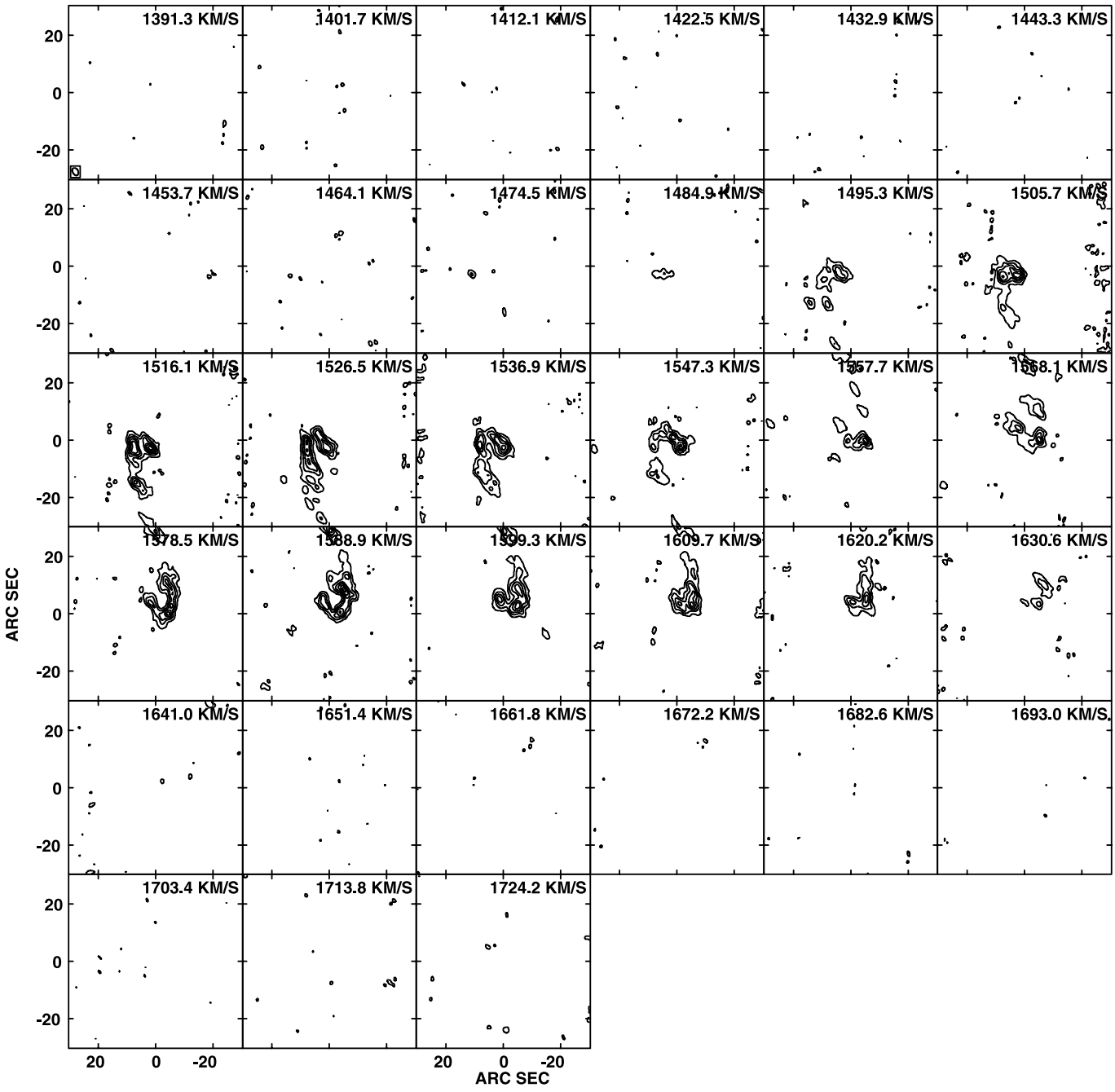

Fig. A1. (Continued.) NGC 4303: Lowest cl = 1.0 K.

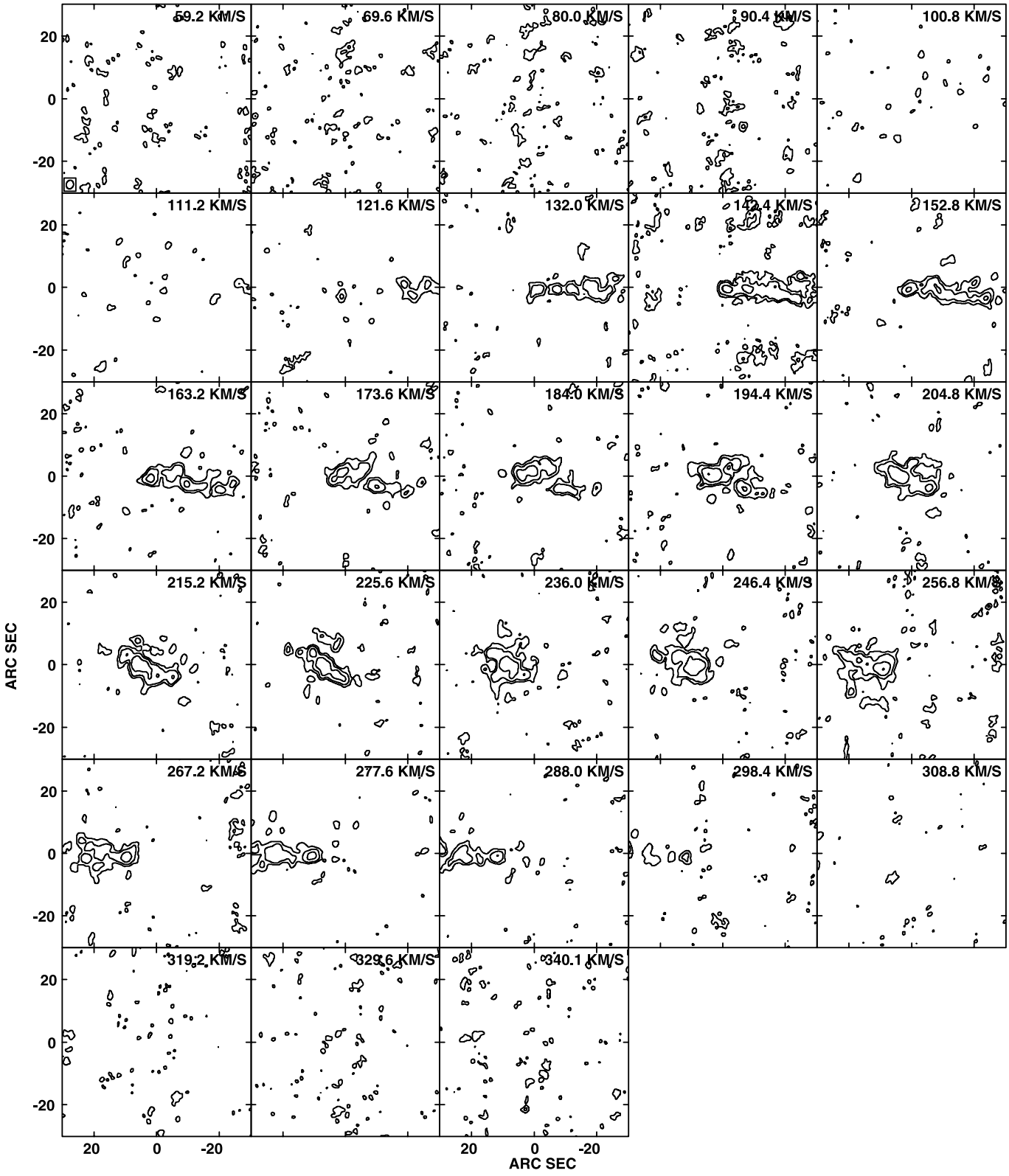

Fig. A1. (Continued.) NGC 4402: Lowest cl = 0.5 K.

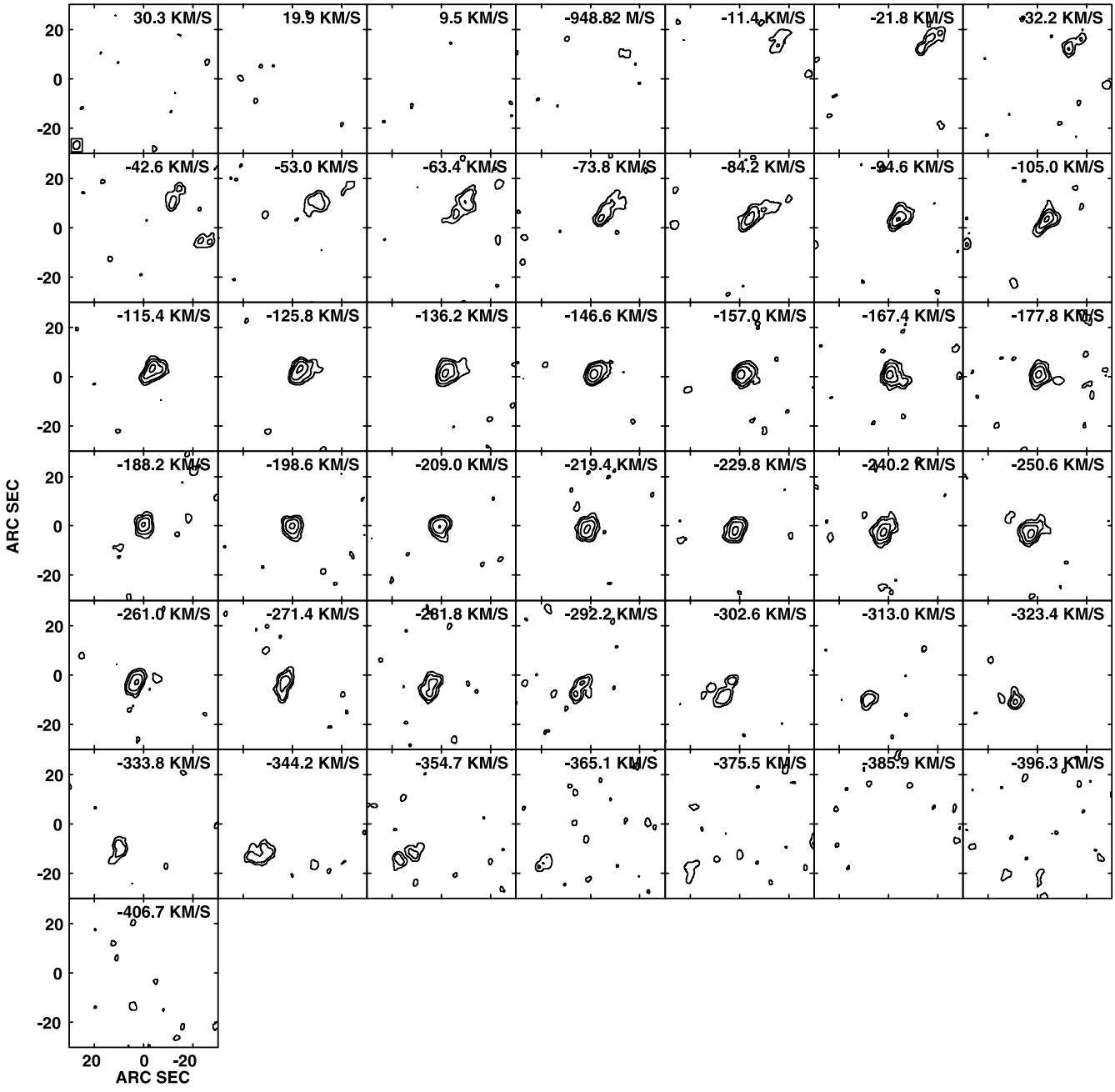

Fig. A1. (Continued.) NGC 4419: Lowest cl = 0.5 K.

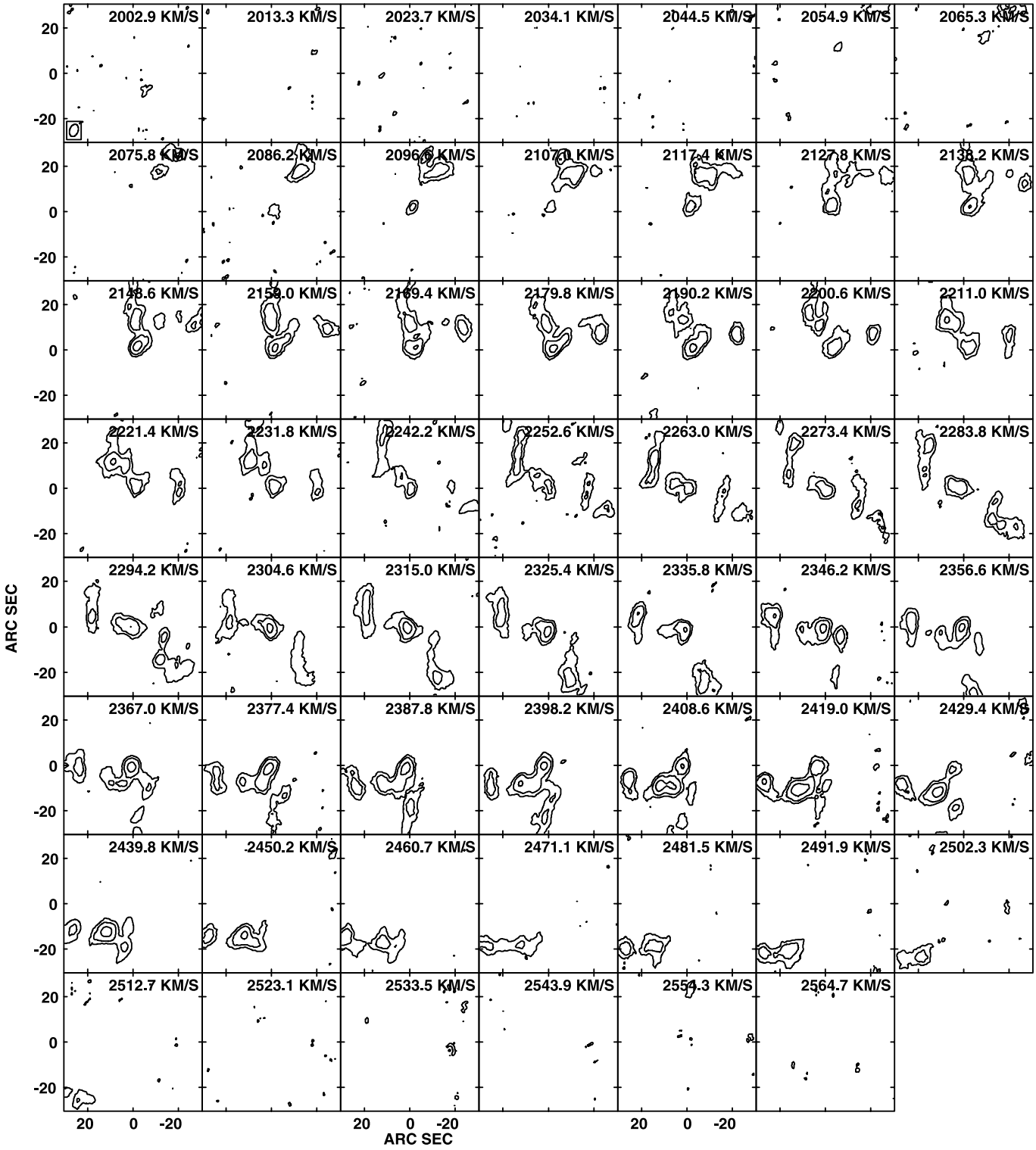

Fig. A1. (Continued.) NGC 4501: Lowest cl = 0.20 K.

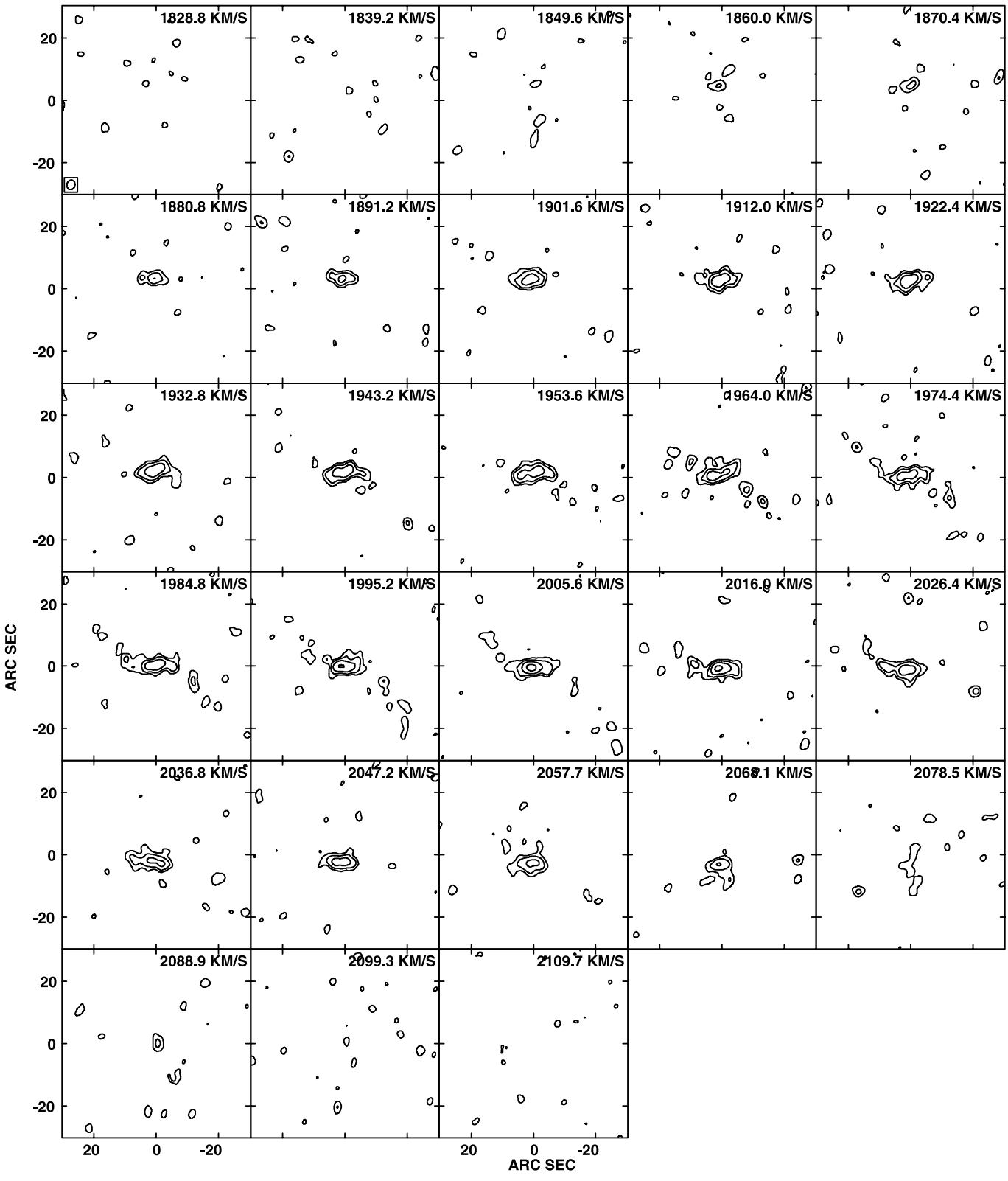

Fig. A1. (Continued.) NGC 4535: Lowest cl = 0.5 K.

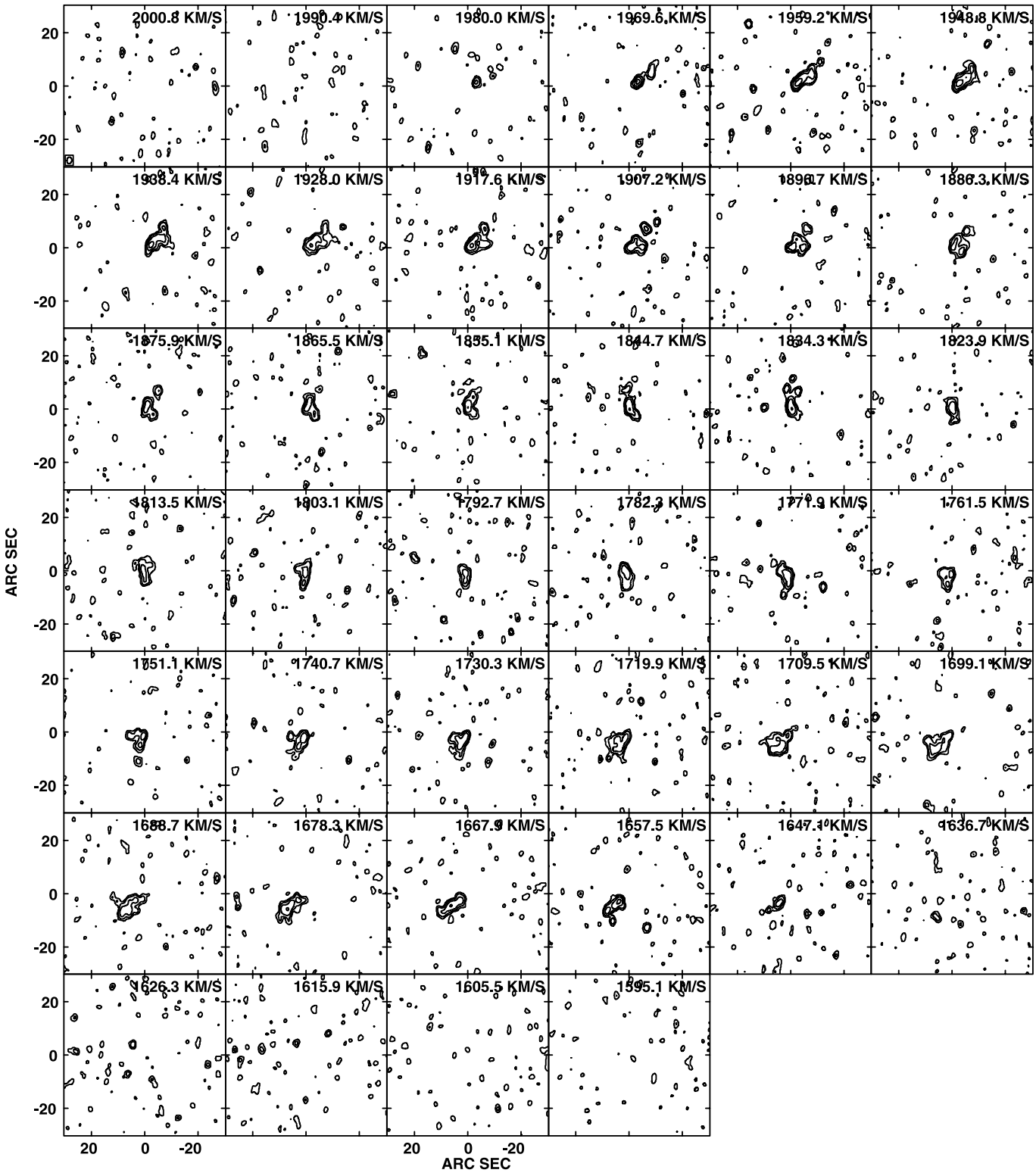

Fig. A1. (Continued.) NGC 4536: Lowest cl = 0.5 K.

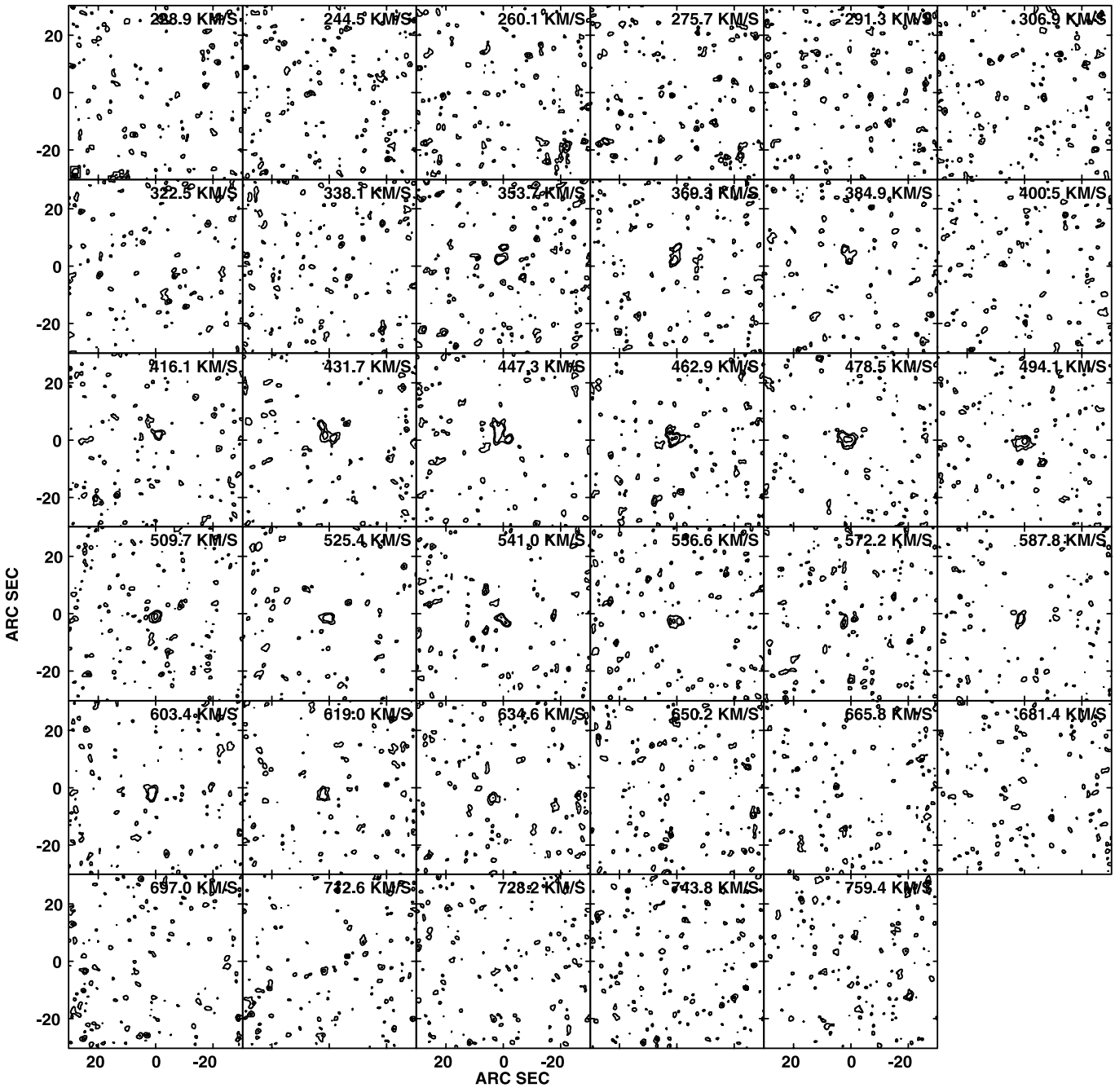

Fig. A1. (Continued.) NGC 4548: Lowest cl = 0.25 K.

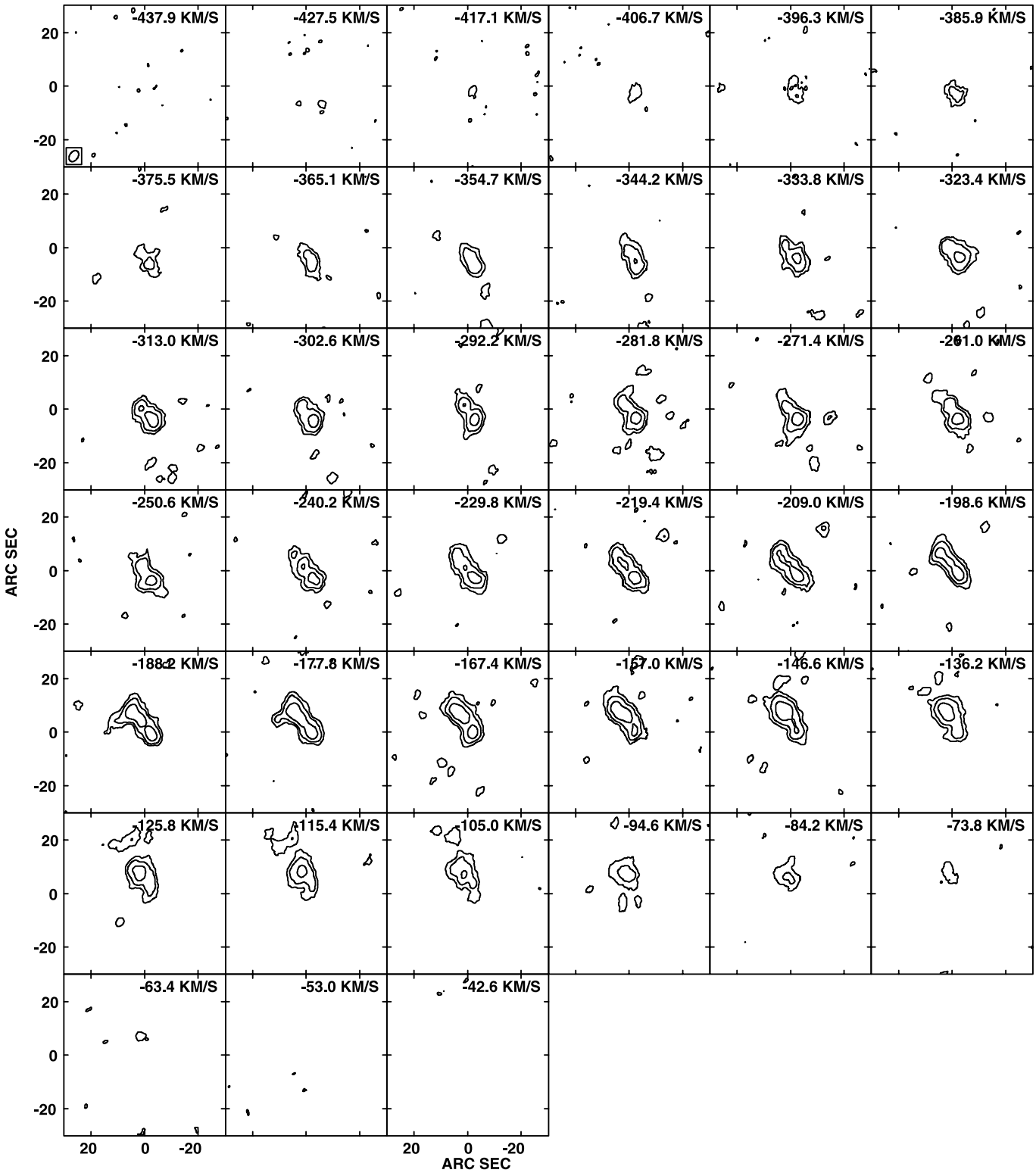

Fig. A1. (Continued.) NGC 4569: Lowest cl = 0.5 K.

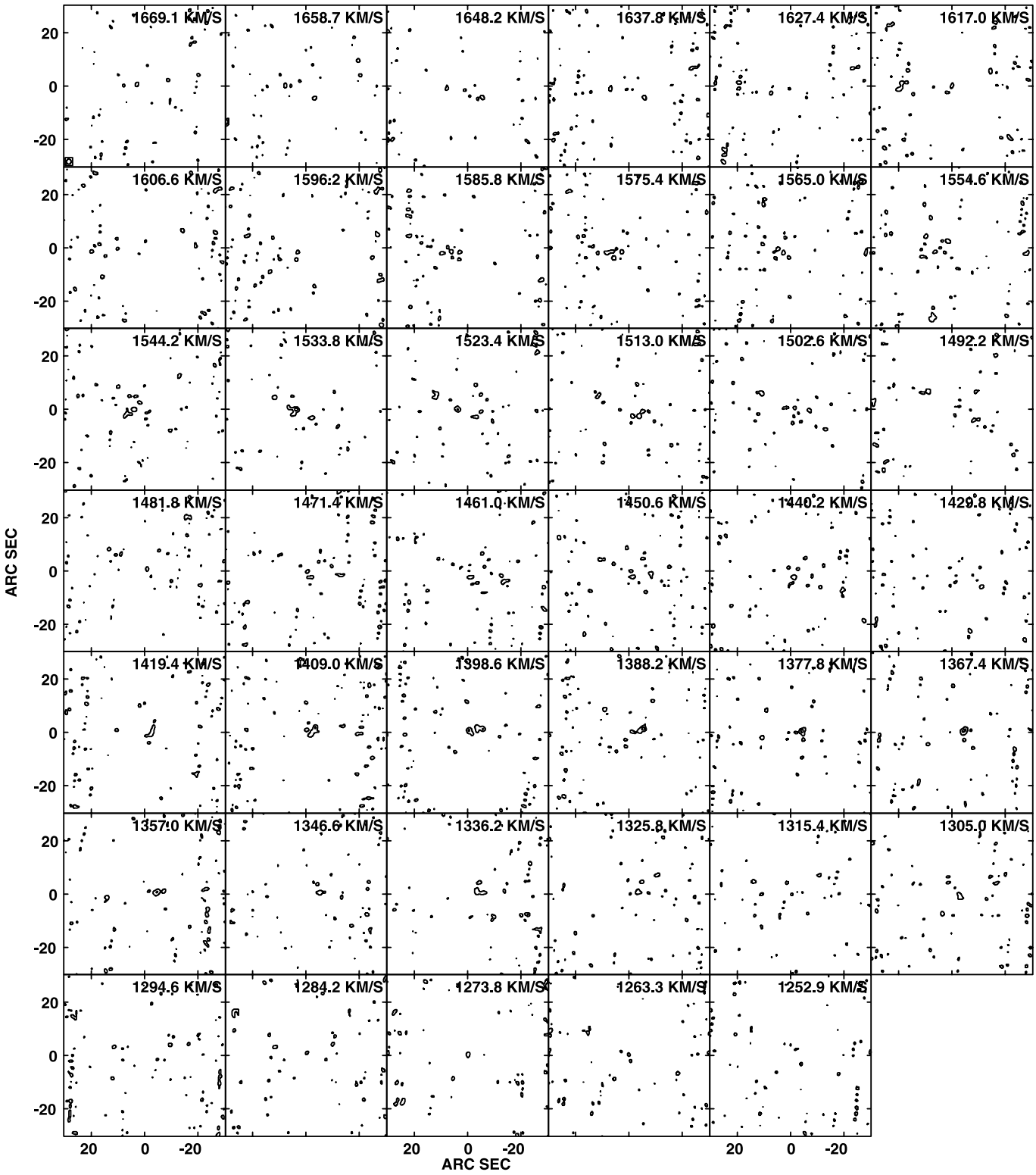

Fig. A1. (Continued.) NGC 4579: Lowest cl = 1.0 K.

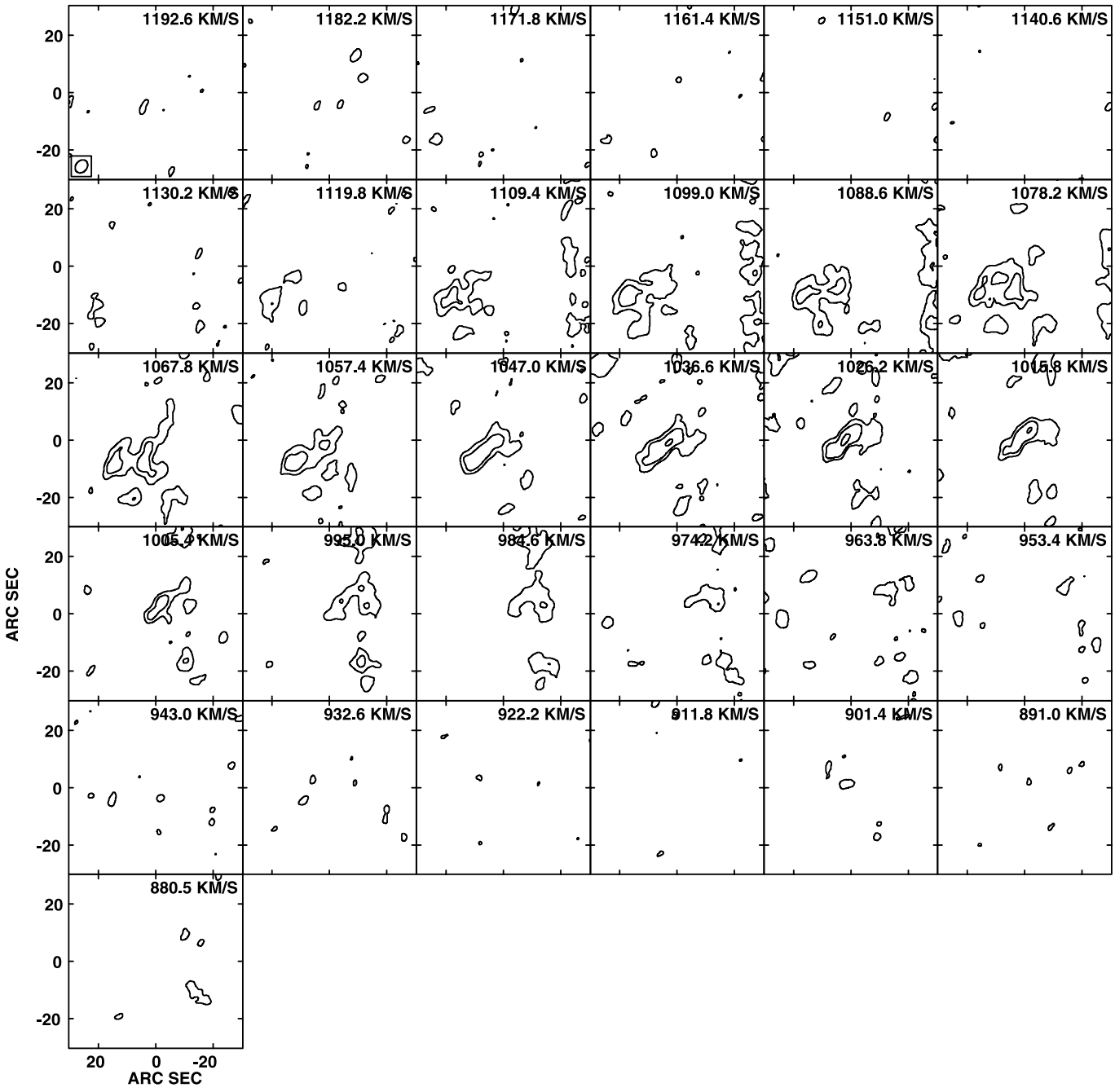

Fig. A1. (Continued.) NGC 4654: Lowest cl = 0.5 K.

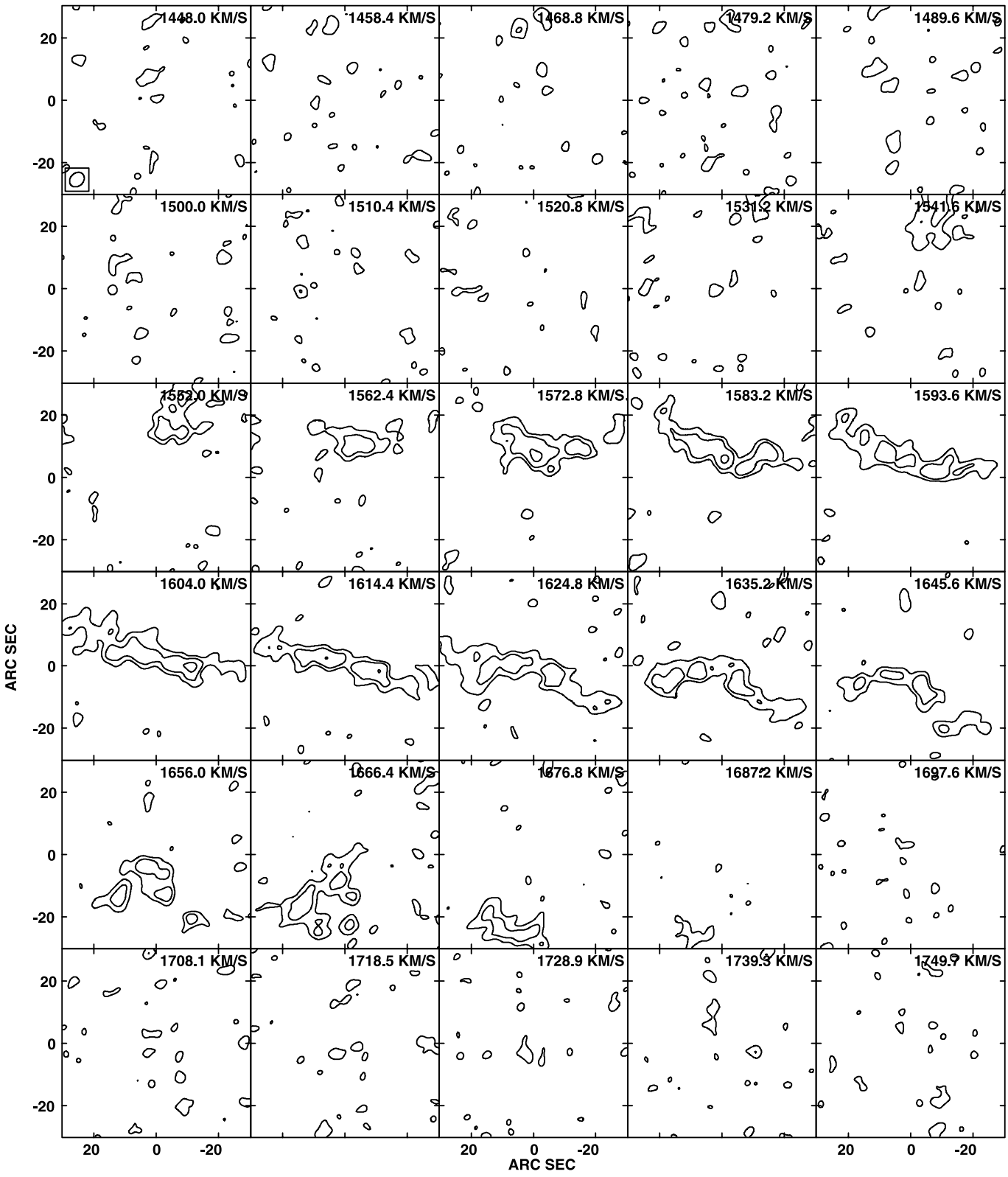

Fig. A1. (Continued.) NGC 4689: Lowest cl = 0.125 K.

References

Baker, A. J. 1999, in The Physics and Chemistry of the Interstellar Medium, ed. V. OssenKopf, J. Stutzki, & G. Winnewisser (Herdecke: GCA-Verlag), 30

Braine, J., Combes, F., Casoli, F., Dupraz, C., Gélin, M., Klein, M., Wielebinsky, R., & Brouillet, N. 1993, A&AS, 97, 887

Brandt, J. C., & Scheer, L. S. 1965, AJ, 70, 471

Cayatte, V., van Gorkom, J. H., Balkowski, C., & Kotanyi, C. 1990, AJ, 100, 604

Condon, J. J., Helou, G., Sanders, D. B., & Soifer, B. T. 1990, ApJS, 73, 359

Cotton, W. D., Condon, J. J., & Arbizzani, E. 1999, ApJS, 125, 409

Ferrarese, L., et al. 1996, ApJ, 464, 568

Fukuda, H., Wada, K., & Habe, A. 1998, MNRAS, 295, 463

Helfer, T. T., et al. 2001, Ap&SS, 276, 1131

Ho, L. C., Filippenko, A. V., & Sargent W. L. W. 1997a, ApJS, 112, 315

Ho, L. C., Filippenko, A. V., & Sargent W. L. W. 1997b, ApJ, 487, 591

Ho, L. C., & Ulvestad, J. S. 2001, ApJS, 133, 77

Honma, M., Sofue, Y., & Arimoto, N. 1995, A&A, 304, 1

Hummel, E., Davies, R. D., Pedlar, A., Wolstencroft, R. D., & van der Hulst, J. M. 1988, A&A, 199, 91

Jogee, S., Baker, A. J., Sakamoto, K., Scoville, N. Z., & Kenney, J. D. P. 2001, in ASP Conf. Ser. Vol. 249, The Central Kiloparsec of Starbursts and AGN, ed. J. H. Knapen, J. E. Beckman, I. Shlosman, & T. J. Mahoney (San Fransisco: ASP), 612

Kenney, J. D., & Young, J. S. 1988, ApJS, 66, 261

Kenney, J. D. P., Young, J. S., Hasegawa, T., & Nakai, N. 1990, ApJ, 353, 460

Kenney, J. D. P., Wilson, C. D., Scoville, N. Z., Devereux, N. A., & Young, J. S. 1992, ApJ, 395, L79

Koda, J., Sofue, Y., Kohno, K., Nakanishi, H., Onodera, S., Okumura, S. K., & Irwin, J. A. 2002, ApJ, 573, 105

Koda, J., & Wada, K. 2002, A&A, 396, 867

Kohno, K., Kawabe, R., & Vila-Vilaró, B. 1999, in The Physics and Chemistry of the Interstellar Medium, ed. V. OssenKopf, J. Stutzki, & G. Winnewisser (Herdecke: GCA-Verlag), 34

Nakanishi, H., Sofue, Y., Koda, J., & Onodera, S. 2003, PASJ, submitted

Nishiyama, K., & Nakai, N. 2001, PASJ, 53, 713

Nishiyama, K., Nakai, N., & Kuno, N. 2001, PASJ, 53, 757

Okumura, S. K., et al. 2000, PASJ, 52, 393

Phookun, B., & Mundy, L. G. 1995, ApJ, 453, 154

Regan, M. W., Thornley, M. D., Helfer, T. T., Sheth, K., Wong, T., Vogel, S. N., Blitz, L., & Bock, D. C.-J. 2001, ApJ, 561, 218

Saikia, D. J., Junor, W., Cornwell, T. J., Muxlow, T. W. B., & Shastri, P. 1990, MNRAS, 245, 408

Sakamoto, K., Okumura, S. K., Ishizuki, S., & Scoville, N. Z. 1999a, ApJS, 124, 403

Sakamoto, K., Okumura, S. K., Ishizuki, S., & Scoville, N. Z. 1999b, ApJ, 525, 691

Sargent, A. I., & Welch, W. J. 1993, ARA&A, 31, 297

Schinnerer, E., Eckart, A., & Tacconi, L. J. 1999, ApJ, 524, L5

Schinnerer, E., Maciejewski, W., Scoville, N., & Moustakas, L. A. 2002, ApJ, 575, 826

Sofue, Y., Honma, M., & Arimoto, N. 1995, A&A, 296, 33

Sofue, Y., Koda, J., Kohno, K., Okumura, S. K., Honma, M., Kawamura, A., & Irwin, J. A. 2001, ApJ, 547, L115

Sofue, Y., Koda, J., Nakanishi, H., & Hidaka, M. 2003b, PASJ, 55, 75

Sofue, Y., Koda, J., Nakanishi, H., & Onodera, S. M. 2003a, PASJ, 55, 59

Sofue, Y., & Rubin, V. 2001, ARA&A, 39, 137

Sofue, Y., Tomita, A., Honma, M., & Tutui, Y. 1999a, PASJ, 51, 737

Sofue, Y., Tutui, Y., Honma, M., Tomita, A., Takamiya, T., Koda, J., & Takeda, Y. 1999b, ApJ, 523, 136

Stark, A. A, Knapp, G. R., Bally, J., Wilson, R. W., Penzias, A. A., & Rowe, H. E. 1986, ApJ, 310, 660

Takamiya, T, & Sofue, Y. 2000, ApJ, 534, 670

Takamiya, T, & Sofue, Y. 2002, ApJ, 576, L15

Terashima, Y., Iyomoto, N., Ho, L. C., & Ptak, A. F. 2002, ApJS, 139, 1

Wada, K., & Habe, A. 1992, MNRAS, 258, 82

Wong, T., & Blitz, L. 2002, ApJ, 569, 157

Young, J. S., & Scoville, N. Z. 1991, ARA&A, 29, 581

Young, J. S., et al. 1995, ApJS, 98, 219